



THE UNIVERSITY *of* EDINBURGH

Edinburgh Research Explorer

Condensate droplet size distribution and heat transfer on hierarchical slippery lubricant infused porous surfaces

Citation for published version:

Maeda, Y, Lv, F, Zhang, P, Takata, Y & Orejon Mantecon, D 2020, 'Condensate droplet size distribution and heat transfer on hierarchical slippery lubricant infused porous surfaces', *Applied Thermal Engineering*, vol. 176, 115386. <https://doi.org/10.1016/j.applthermaleng.2020.115386>

Digital Object Identifier (DOI):

[10.1016/j.applthermaleng.2020.115386](https://doi.org/10.1016/j.applthermaleng.2020.115386)

Link:

[Link to publication record in Edinburgh Research Explorer](#)

Document Version:

Peer reviewed version

Published In:

Applied Thermal Engineering

General rights

Copyright for the publications made accessible via the Edinburgh Research Explorer is retained by the author(s) and / or other copyright owners and it is a condition of accessing these publications that users recognise and abide by the legal requirements associated with these rights.

Take down policy

The University of Edinburgh has made every reasonable effort to ensure that Edinburgh Research Explorer content complies with UK legislation. If you believe that the public display of this file breaches copyright please contact openaccess@ed.ac.uk providing details, and we will remove access to the work immediately and investigate your claim.



Condensate Droplet Size Distribution and Heat Transfer on Hierarchical Slippery Lubricant Infused Porous Surfaces

Yota Maeda¹, Fengyong Lv^{2,3}, Peng Zhang², Yasuyuki Takata^{1,4}, Daniel Orejon^{4,5} *

¹Department of Mechanical Engineering, Thermofluid Physics Laboratory, Kyushu University, 744 Motooka, Nishi-ku, Fukuoka 819-0395, Japan

²Institute of Refrigeration and Cryogenics, Shanghai Jiao Tong University, Shanghai 200240, China

³College of Urban Construction and Safety Engineering, Shanghai Institute of Technology, Shanghai 201418, China

⁴International Institute for Carbon-Neutral Energy Research (WPI-I²CNER), Kyushu University, 744 Motooka, Nishi-ku, Fukuoka 819-0395, Japan

⁵Institute for Multiscale Thermofluids, School of Engineering, The University of Edinburgh, Edinburgh EH9 3FD, Scotland, UK

* Corresponding author: d.orejon@ed.ac.uk

Abstract

In recent years, slippery lubricant infused porous surfaces (SLIPSs) have received important attention due to their excellent performance in applications such as condensation, low friction, self-cleaning and anti-icing, which is owed to the presence of an infused lubricant or oil effectively decreasing the liquid-solid interactions and enhancing droplet mobility when compared to hydrophobic and/or to superhydrophobic surfaces. In this work, we fabricate and make use of hierarchical micro-/nano-structured and nano-structured SLIPSs for condensation phase-change. Optical microscopy and macroscopic experimental observations are coupled to extract the droplet size distribution at different condensation times. Heat transfer resistance

model through individual condensing droplets is further extended here to account for the presence of both micro- and nano-structures. Then, heat transfer through individual droplets is coupled to the droplet number density to estimate the heat transfer at different condensation times and their overall performance. A 100% greater heat transfer performance is reported on nano-structured SLIPs when compared to hierarchical micro-/nano-structure SLIPs due to the greater thermal resistance imposed by the micro-structures and the lubricant present within the structures. We conclude that although the presence of micro-structures shifts the droplet number density towards greater population of smaller sized droplets, this effect is not enough to overcome the greater heat transfer predicted on solely nano-structured SLIPs. Findings presented here complement current research on SLIPs and condensation phase-change and are of great importance for the effective design of SLIPs with enhanced condensation heat transfer performance.

Keywords: Slippery Lubricant Infused Porous Surfaces, Condensation Phase-Change, Heat Transfer, Hierarchical SLIPs, Droplet Size Distribution, Heat Transfer Resistance Based Model

Nomenclature

Variables

S_{RMS}	average surface roughness [μm]
S_z	distance between the highest top and the lowest valley [μm]
f	solid fraction [-]
f_n	solid fraction of nano-structures [-]
φ_m	solid fraction of micro-structures [-]
θ_a	advancing contact angle [$^\circ$]
θ_i	intrinsic contact angle on the flat hydrophobic surface [$^\circ$]
θ_r	receding contact angle [$^\circ$]
θ_e	average contact angle [$^\circ$]
θ_{a_SHS}	advancing angle on SHS [$^\circ$]
r	droplet radius [m]
r_e	effective droplet radius [m]
r_{range}	average droplet radius between the two extremes of the size range [m]
r_{min}	minimum radius for nucleation [m]
r_{max}	maximum experimental radius [mm]
T_{amb}	ambient temperature [K or $^\circ\text{C}$]
T_{sub}	substrate temperature [K or $^\circ\text{C}$]
T_{sat}	saturation temperature [K or $^\circ\text{C}$]
ΔT	subcooling condition [K]
ΔT_c	difference of temperature due to the Kelvin effect [K]
RH	relative humidity [%]
N_s	nucleation density before coalescence [#/ mm^2]
$n(r)$	droplet number density for sizes below the effective radius r_e [#/ mm^3]
$N(r)$	droplet number density for sizes above the effective radius r_e [#/ mm^3]
$N_{\text{re}}(r)$	number of droplets of certain radius r [#]
A	area of observation [mm]
t	time [min]
γ_{wa}	surface tension water-air [N/m]
ρ_w	density of the condensate [kg/m^3]
h_{fg}	latent heat of condensation [kJ/kg]
q''	theoretical surface heat flux [W/m^2]
q_d	heat transfer individual droplets [W]

$q_{d/n/c/l}$	heat transfer on nano-structured SLIPS [W]
$q_{d/m/n/c/l}$	heat transfer on micro-/nano-structured SLIPS [W]
R_i	interfacial thermal resistance for condensation [K/W]
R_d	droplet thermal resistance [K/W]
R_l	lubricant thermal resistance [K/W]
R_{Cu}	micro-structure thermal resistance [K/W]
$R_{m/n/c/l}$	micro-/nano-structures, hydrophobic coating and lubricant resistance [K/W]
$R_{n/c/l}$	nano-structures, hydrophobic coating and lubricant thermal resistance [K/W]
h_i	condensation interfacial heat transfer coefficient [$\text{W}/\text{m}^2/\text{K}$]
α	accommodation coefficient [-]
R_g	specific gas constant [J/kg/K]
ρ_v	water vapour specific density [kg/m^3]
k_w	water thermal resistance [W/m/K]
δ_l	thickness of the lubricant [m]
k_l	thermal conductivity of the lubricant [W/m/K]
δ_c	thickness of the hydrophobic coating [m]
k_c	thermal conductivity of the hydrophobic coating [W/m/K]
h_{CuO}	height of the nano-structures [m]
k_{CuO}	thermal conductivity of the copper oxide [W/m/K]
h_{Cu}	height of micro-structures [m]
k_{Cu}	thermal conductivity of copper [W/m/K]
a	droplet number density coefficient [-]
b	droplet number density slope [-]

Abbreviations

SLIPS	Slippery Lubricant Infused Porous Surface
SHS	Superhydrophobic Surface
FWC	Filmwise Condensation
DWC	Dropwise Condensation
VOCs	Volatile Organic Compounds
CAH	Contact Angle Hysteresis [$^\circ$]
SI	Supplementary Information
GPL	General Purposes Lubricant
1D	One Dimensional

1 **Introduction**

2 Industrial and everyday applications such as power generation, air conditioning and electronics
3 cooling rely on filmwise condensation (FWC) as the main condensation mechanism. FWC
4 ensues on high surface energy materials such as copper, aluminium, titanium or stainless steel
5 typically employed on the condenser side [1, 2]. Nonetheless, in the past decades, aiming to
6 improve the heat transfer performance of the condenser, researchers have made use of
7 hydrophobic coatings that can lower the energy of the surface prompting the continuous
8 nucleation, growth and departure of the condensate via gravitational forces in a dropwise
9 condensation (DWC) fashion[3-6]. Owing to the continuous condensate removal of millimetre
10 droplets, DWC on hydrophobic surfaces provides greater heat transfer coefficients than FWC
11 [7-9]. In addition to hydrophobic surfaces, micro-/nano-textured surfaces coated with a thin
12 conformal hydrophobic layer, so called superhydrophobic surfaces (SHSs), have demonstrated
13 to provide excellent low adhesion and enhanced condensation heat transfer performance when
14 compared to both hydrophilic and hydrophobic surfaces [10-12]. While on hydrophobic
15 surfaces droplets must grow to sizes in the order of a millimetre before the condensate sheds
16 the surface, the extreme low adhesion of the condensate to SHSs can ensue removal of droplets
17 via gravity and coalescence-induced droplet-jumping of droplets with sizes in the
18 submillimetre/micrometre range [11, 13, 14] or even in the submicron range [15]. SHSs can
19 enhance the overall condensation heat transfer performance up to 25% when compared to DWC
20 on hydrophobic surfaces and up to 5 times when compared to FWC [11, 16, 17]. We note here
21 that most heat transfer via condensation takes place for droplet sizes in the submillimetre range
22 [2, 18, 19].

23 The excellent condensation heat transfer, water repellency, anti-fogging and anti-icing
24 properties of SHSs are owed to the presence of air pockets entrapped within the hydrophobic
25 micro- and/or nano-structures, which effectively decrease the solid-liquid binary interactions

26 and hence the adhesion of the condensate to the surface [20, 21]. In addition to SHSs,
27 hydrophilic micropillared surfaces [22], hydrophobic-hydrophilic patterned wettability
28 surfaces [23, 24], surfaces with amphiphilic micro-structures (hydrophilic micropillars with
29 hydrophobic tops) [25, 26], nano-structured porous surfaces coated with a hydrophobic
30 promoter layer [27], and/or superhydrophobic/superhydrophilic patterned wettability surfaces
31 [14, 28, 29], are other approaches adopted for the control of the condensate aiming to improve
32 the heat transfer performance during phase-change. More recently, continuous nucleation,
33 growth and departure of droplets via gravity and/or coalescence-induced droplet-jumping in a
34 DWC fashion was achieved on bare structured micro- and nano-structured copper oxide
35 surfaces exposed to the ambient [30, 31]. Upon exposure to laboratory conditions, the
36 adsorption of hydrophobic volatile organic compounds (VOCs) onto the copper oxide nano-
37 structures mask the intrinsic hydrophilic wettability of the metal empowering the
38 superhydrophobic properties of such engineered surfaces [30, 31]. The transition from
39 hydrophilic to hydrophobic upon adsorption of VOCs was earlier reported on smooth metals
40 and rare earth oxides by Preston *et al.* [32] while the transition from hydrophilic to
41 superhydrophobic on boron nitride nanotubes was reported by Boinovich *et al.* [33].

42 If we now impregnate the micro- and/or the nano-structures of a SHS with a lubricant or an
43 oil, a new range of low adhesion water-repellent surfaces coined slippery lubricant infused
44 porous surfaces (SLIPSs) emerge [34, 35]. SLIPSs have been reported to provide extremely
45 low adhesion between the liquid and the infused surface, prompting droplet self-removal for
46 surface inclination angles as low as 5° , and offering very low contact angle hysteresis *ca.* 2.5°
47 [36-38]. SLIPSs offer virtually no-pinning due to the smoothness of the lubricant layer and to
48 the more affinity of the lubricant for the surface, *i.e.*, for the hydrophobic coating, hindering
49 the condensate substrate intimate interactions [37, 39, 40]. Furthermore, SLIPSs surfaces can
50 overcome the high adhesion of droplets sitting in the Wenzel state as per the recently reported

51 slippery Wenzel state on lubricant infused hierarchical micro- and nano-textured SLIPsSs[13].
52 Some of the applications where SLIPsSs excel are self-cleaning [41], drag reduction [42], anti-
53 icing [43], water harvesting [44], along with their self-healing capabilities [35]. In addition to
54 the abovementioned applications, SLIPsSs are excellent candidates for condensation heat
55 transfer providing up to 100% greater heat transfer coefficients for water when compared to
56 hydrophobic and/or to SHSs [45], and 400% and 450% enhancement when compared to FWC
57 for water and toluene, respectively [46]. The excellent low adhesion of SLIPsSs performing in
58 a DWC manner has also been proven even for low surface tension fluids such as: octane,
59 hexane and pentane [39]. Thereafter, Weisensee *et al.* provided a coupled experimental and
60 analytical methodology for the estimation of the heat transfer performance on SLIPsSs as a
61 function of the coating thickness and the solid fraction, reporting ca. 12 times better heat
62 transfer when compared to FWC [2]. More recently, continuous DWC of low surface tension
63 ethanol with the consequent enhancement in heat transfer performance has been reported on
64 functionalised copper oxide nanostructured surfaces infused with Krytox™ 1525 lubricant [47].
65 To recap, SLIPsSs present important advantages when compared to hydrophobic surfaces and
66 to SHSs such as: occurrence of DWC for low-surface tension fluids with quick droplet
67 shedding opposed to FWC taking place on hydrophobic surfaces or SHSs [39, 46, 47];
68 occurrence of slippery Wenzel state while on SHSs droplets remain pinned to the structures,
69 i.e., rose petal state [48]; self-healing properties as the lubricant film can wick into lubricant
70 depleted zones or within structural damaged areas [35]; presence of a protective lubricant layer
71 against corrosion preventing the direct interaction between the environment and the structured
72 surface underneath the oil[49], as well as anti-icing [43] and anti-fouling and/or anti-scale [50]
73 enhanced capabilities, owed to the reduced adhesion and interactions, etc. More specifically,
74 in the context of this manuscript, we make use of SLIPsSs as per their enhanced droplet mobility

75 of small droplets, i.e., greater droplet removal frequency, and enhanced droplet shedding
76 velocities when compared to hydrophobic surfaces and to SHSs [51].

77 Aiming to better understand the interactions between fluids and SLIPs, lubricant viscosity
78 [2, 37, 48, 52], presence or absence of nano-structures on a micropillared surface [51], and the
79 spacing between micro-structures [37], are some of the parameters previously addressed in the
80 literature. The viscosity of the lubricant affects droplet mobility with greater shedding
81 velocities in the case of low surface tension lubricants either upon droplet deposition on an
82 inclined surface [37, 52] or during dynamic condensation [2, 39]. Smith *et al.* investigated the
83 effect of micro-structure spacing upon droplet deposition on micro-posts (in absence of a nano-
84 scale roughness) reporting a decrease in the roll-off angle as the spacing was increased [37].
85 By increasing the surface roughness, i.e., decreasing the solid fraction, Dai *et al.*, observed an
86 increase in the apparent contact angle of deposited water droplets, which can be directly
87 associated with a decrease in the effective droplet-SLIPs adhesion[43]. Anand *et al.*,
88 compared the condensation behaviour on a micro-/nano-structured SHS to that of a micro-
89 /nano-structured SLIP [51]. They reported on the effective droplet mobility of droplets below
90 the submillimetre range on SLIPs; whereas on SHSs, droplets with sizes above 3 millimetres
91 were necessary in order to overcome the adhesion to the surface [51]. On other hand, a 10 fold
92 increase in the amount of condensate collected was reported for condensation on slippery
93 asymmetric bumps by combining the macroscopic bumps of the desert beetle with the
94 asymmetric features of a cactus spine and with the slippery nature of the pitcher plant when
95 compared to a flat SLIPs [53]. From the above literature, it is clear that the surface structure
96 induces different droplet-surface adhesion as exemplified by the different apparent and rolling
97 angles reported when increasing the spacing between structures, i.e., when decreasing the solid
98 fraction [37, 48]. In essence, in this work, two cases where the effective area fraction is
99 decreased as a consequence of the presence of micro-structures and lubricant oil present within

100 them are compared to two other cases with absence of micro-structures. In addition, and despite
101 of the extensive amount of experimental research carried out in the past 9 years on the
102 fundamentals of droplets on SLIPSs and on applied heat transfer, the presence of micro-
103 structures as in the work of Anand et al. [51] and the absence of micro-structures underneath
104 the infused lubricant as in the work of Weisensee et al. [2] during condensation have not been
105 compared to date. Hence, in the present work, we make use of SLIPSs fabricated following
106 facile and easy scalable etching and oxidation procedure as in the work of Zhu *et al.*, and in
107 our earlier works [54-57].

108 In the present work, two different SHSs varying in the size and density of the micro-
109 structures, *i.e.*, big size and high density of micro-structures and small size and low density of
110 micro-structures, were prepared. In addition, two nano-structured SHSs with similar size and
111 density of the nano-structures were also fabricated. After fabrication, SHSs were infused with
112 a low energy lubricant to create our SLIPSs. Finally, the condensation performance on all four
113 SLIPSs was addressed inside an environmental chamber by means of optical microscopy and
114 macroscopic experimental observations. From optical microscopy and macroscopic
115 experimental observations, the droplet number density, $N(r)$ [#/ mm^3] at different time intervals
116 on the different SLIPSs, was extracted. Then, to estimate the overall heat transfer performance,
117 the droplet number density is coupled with steady-state heat transfer conduction analysis
118 through individual droplets. The heat transfer model adopted here has been extended to account
119 for the presence of both micro- and nano-structures, contrasting to earlier models where only
120 the micro-structures [58] or the nano-structures on a SHS [9, 18] and on a SLIPS [2] were
121 considered. Results show the better overall theoretical heat transfer performance of up to 100%
122 increase on nano-structured surfaces when compared to hierarchical micro-/nano-structured
123 SLIPSs. The worse heat transfer performance in the presence of micro-structures is owed to
124 the additional heat transfer resistance imposed by the greater thickness of the micro-structures

125 and the impregnated lubricant present within the micro-structures. Although the presence of
126 micro-structures seems to shift the droplet size distribution towards greater droplet size
127 numbers and smaller sizes, differences on the theoretical heat transfer through single droplets
128 outweigh that of the droplet number density at any given time. Last, the periodicity of the
129 theoretical heat transfer calculations based on the different droplet number densities reported
130 at different condensation times as a consequence of the continuous nucleation, growth and
131 shedding of droplets in a DWC is presented and discussed for the first time. We conclude here
132 on the greater overall theoretical heat transfer on solely nano-structured surfaces independent
133 of the condensation time. Nonetheless, we would like to note that the observed shift of the
134 droplet number density towards smaller droplet sizes on hierarchical micro-/nano-structured
135 SLIPS, presumably due to the lower adhesion to the surface, might in turn induce quicker
136 droplet shedding and improved heat transfer performance not captured by the overall
137 theoretical heat transfer resistance based model.

139 **Experimental Procedure**

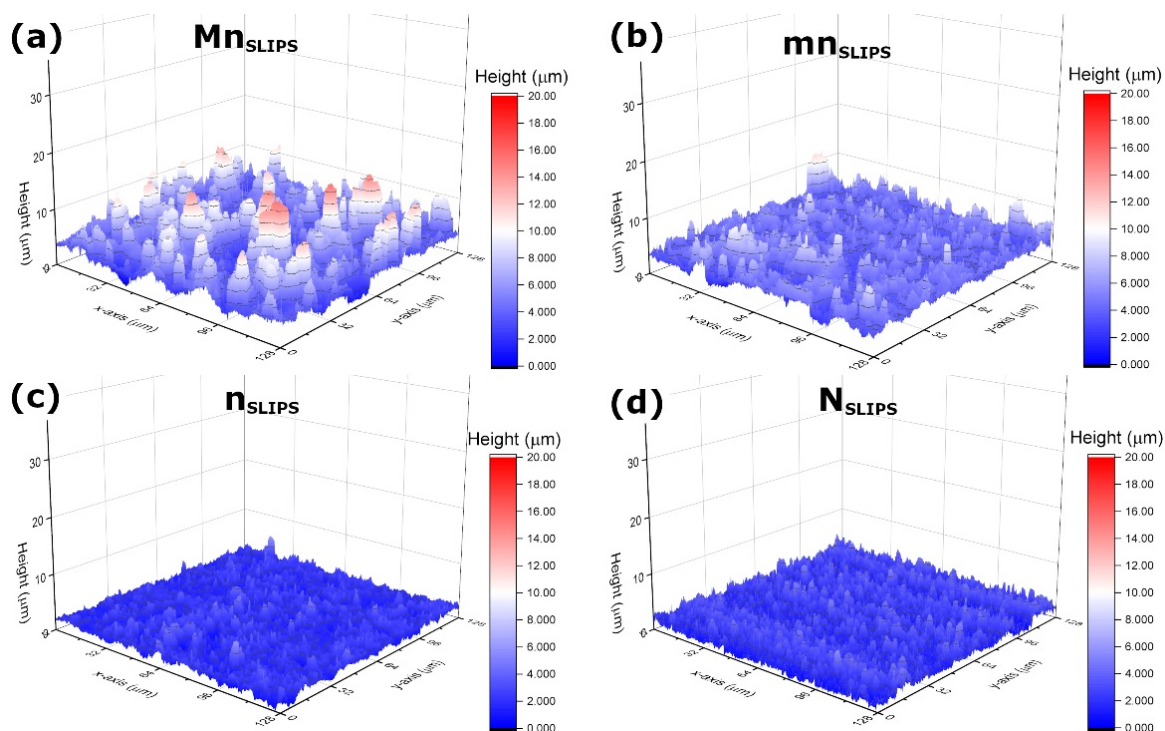
140 **Surface fabrication**

141 Two hierarchical micro- and nano-structured SHSs varying in the size and the density of the
142 micro-structures were fabricated as in the work of Zhu *et al.* and Zhang *et al.* [54, 55, 57].
143 Pristine copper plates of 10 x 10 mm² and 500 μm in thickness were ultrasonicated in acetone,
144 then in ethanol and lastly in distilled water prior to drying by nitrogen gas to remove any
145 contaminant. Then, surfaces were immersed in a solution of 10 wt. % of HCl-H₂O to remove
146 the oxide layer. Thereafter, samples were further cleaned in an ultrasonic bath with distilled
147 water followed by drying with nitrogen gas. To create the different size and density of the
148 micro-structures, samples were subjected to a easily-scalable wet etching in 0.48 wt % H₂O₂-
149 H₂O and 1.89 mol/L HCl-H₂O solution as in Ref. 59 [59]. Bigger size and greater density of
150 the micro-structures were conferred by dipping the copper substrate for longer time and at
151 higher temperature (1 hour at 60 °C versus 20 minutes at 17 °C) [55, 57]. Next, to provide the
152 surfaces with the necessary nanoscale roughness for the effective infusion and stability of the
153 lubricant, both etched substrates were further oxidized in an aqueous solution of 2.5 mol/L
154 NaOH-H₂O and 0.1 mol/L ((NH)₄S₂O₈-H₂O) for 30 minutes at 70 °C [54, 55]. In addition, to
155 allow for comparison between hierarchical micro-/nano-structured SLIPSs to solely nano-
156 structured ones, smooth copper plates, i.e., non-etched samples, were further oxidized in the
157 same aqueous solution of 2.5 mol/L NaOH-H₂O and 0.1 mol/L ((NH)₄S₂O₈-H₂O) for 30
158 minutes at 70 °C (as the micro-structured ones) and for 50 minutes at 15 °C. We henceforth
159 refer to the hierarchical micro-/nano-structured SLIPSs as Mn_{SLIPS} for high density and big size
160 of micro-structures and as mn_{SLIPS} for small size and low density of micro-structures. While
161 solely nanostructured SLIPSs are referred as n_{SLIPS} for the small size blade-like of
162 nanostructures (similar to those on Mn_{SLIPS} and mn_{SLIPS}) and N_{SLIPS} for the large size needle-
163 like nanostructures. After surface oxidation, all samples were immersed in a solution of 1%
164 POTS(1H,1H,2H,2H-Perfluorooctyltriethoxysilane)-ethanol for 12 hours at ambient

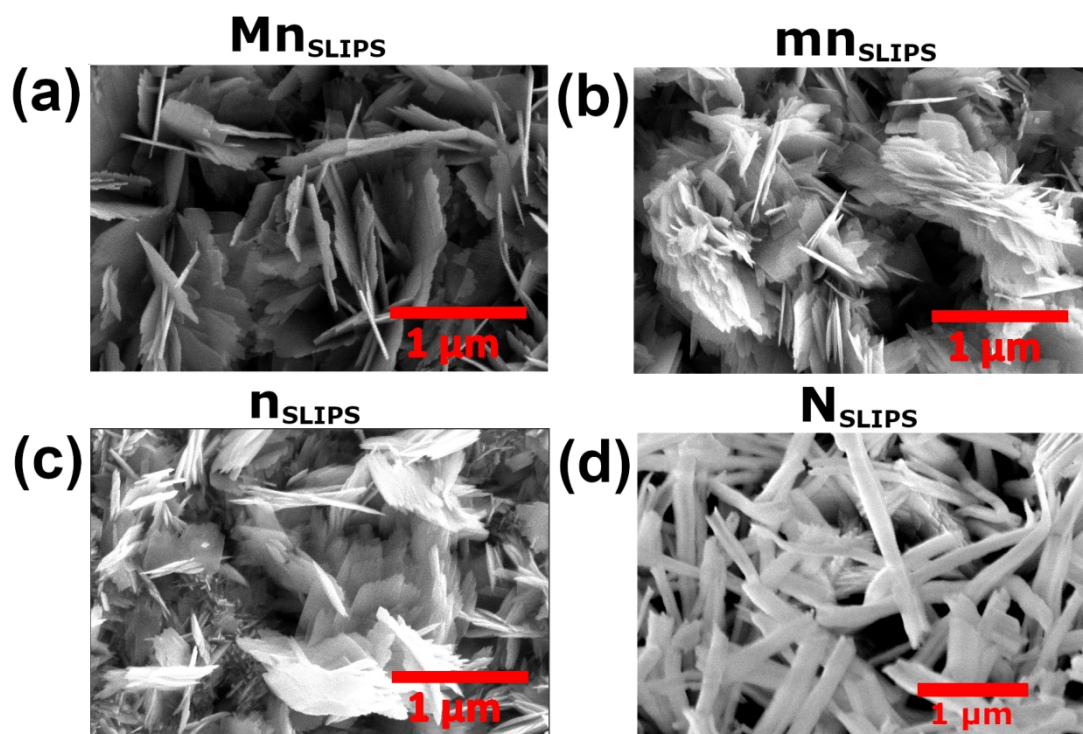
165 temperature, rendering the intrinsic wettability of the micro- and the nano-structures
166 hydrophobic [60, 61]. We note here that the hydrophobicity of the nano-structures is a
167 necessary condition on the here fabricated SLIPSs in order to induce the more wetting affinity
168 of the lubricant to the surface when compared to water [57]. All chemicals used during the
169 fabrication procedure were purchased from Sinopharm Chemical Reagent Co., Ltd. (China).

170 **Characterisation of SLIPSs before impregnation**

171 The micro- and the nano-structure topography of Mn_{SLIPS} , mn_{SLIPS} , n_{SLIPS} and N_{SLIPS} before
172 lubricant impregnation was assessed via Laser Optical Microscopy in a LEXT OLS4000 3D
173 Laser Measuring Microscope from Olympus (Japan), and via Scanning Electron Microscopy
174 (SEM) in a 3D Versa Dual Beam Environmental Scanning Electron Microscope from FEI
175 Company (Hillsboro, Oregon, USA), respectively. Figure 1 includes 3D Laser Optical
176 Microscopy profiles giving account of the different size and density of the micro-structures,
177 while Figure 2 shows the surface nano-structures decorating the different surfaces:



178
179 **Figure 1 - 3D Laser Optical Microscopy on (a) Mn_{SLIPS} , (b) mn_{SLIPS} , (c) n_{SLIPS} and (d) N_{SLIPS} , prior**
180 **to impregnation. Field of view is $128 \times 128 \mu m^2$ with a maximum height profile of $20 \mu m$. Scale**
181 **intensity of the height of the 3D surface profile changes from deep blue ($0 \mu m$) to red ($20 \mu m$).**



182

183 **Figure 2 – High magnification Scanning Electron Microscopy (SEM) of the nanostructures**
 184 **decorating superhydrophobic (a) Mn_{SLIPS} , (b) mn_{SLIPS} , (c) n_{SLIPS} and (d) N_{SLIPS} , prior to**
 185 **impregnation. Scale bar is 1 μm .**

186

187

188

189

190

191

192

193

194

195

196

197

From 3D Laser Optical Microscopy profiles presented in Figure 1, on one hand the greater size and density of the micro-structures on Mn_{SLIPS} (Figure 1a) when compared to mn_{SLIPS} (Figure 1b) is evident. Structures with height and lateral dimensions in the order of 20 micrometres are reported on Mn_{SLIPS} , while on mn_{SLIPS} height and lateral dimensions are kept below 10 micrometres as a consequence of the lesser time and lower temperature of the etching process. On the other hand, the absence of flower like micro-structures on n_{SLIPS} (Figure 1c) and on N_{SLIPS} (Figure 1d) when compared to Mn_{SLIPS} (Figure 1a) and mn_{SLIPS} (Figure 1b) is highlighted. Further surface characterisation including 2D Laser Optical Microscopy profiles of the four SLIPSs studied can be found in and Figure SI1 and Section SI.1 in the accompanying Supplementary Information (SI). When looking into the surface nano-structures included in Figure 2, of importance is to stress the similar geometry, size and density of the nano-structures decorating Mn_{SLIPS} (Figure 2a), mn_{SLIPS} (Figure 2b) and n_{SLIPS} (Figure 2c), which is owed to

218 the very same oxidation procedure followed. When comparing Mn_{SLIPS} (Figure 2a), mn_{SLIPS}
219 (Figure 2b) and n_{SLIPS} (Figure 2c) to N_{SLIPS} (Figure 2d) though, clear differences on the
200 geometry (blade-like versus needle-like nano-structures) while slight differences on the
201 random arrangement are revealed.

202 To provide further characterisation on the different surface structure depending on the
203 fabrication procedure, the average surface roughness S_{RMS} and the distance between the highest
204 top and the lowest valley S_z were extracted from 3D Laser Optical Microscopy, which are
205 included in Table 1. In addition, the solid fraction f before impregnation was estimated making
206 use of the Cassie-Baxter equation as $f = (\cos \theta_{a_SHS} + 1)/(\cos \theta_i + 1)$ [55, 62], where θ_{a_SHS}
207 is the advancing contact angle of the superhydrophobic surface without impregnation and θ_i is
208 the intrinsic contact angle on the flat hydrophobic surface equals $115^\circ \pm 3^\circ$ [55]. The solid
209 fraction f for each of the structured surfaces fabricated before impregnation is then included in
210 Table 1. We note here that all surfaces before impregnation showed superhydrophobicity with
211 advancing contact angles above 155° as earlier reported [55].

212 **Characterisation of SLIPSs**

213 After etching, oxidation and hydrophobization of the surfaces, coated samples were immersed
214 in Krytox[®] General Purpose Lubricant 103 (GPL103) from DuPont[™] (USA). GPL103 has a
215 density of 1.92 kg/dm^3 at 0°C and a viscosity of 82 cSt at 20°C . Next, advancing contact
216 angle, θ_a ($^\circ$), and receding contact angle, θ_r ($^\circ$), of the fabricated SLIPSs after impregnation
217 were measured in a custom-built goniometer and analysed using ImageJ snake-based approach
218 plugging [63, 64]. θ_a and θ_r were extracted from the shape of 3 microliter droplet sliding over
219 the different SLIPSs, which are included in Table 1. Standard deviations on θ_a , and θ_r were
220 obtained from 3 independent experiments.

221

222 **Table 1 – Substrate characterization of Mn_{SLIPS} , mn_{SLIPS} , n_{SLIPS} and N_{SLIPS} as: S_{RMS} surface**
 223 **roughness (μm), S_z maximum distance between highest top and lowest valley of the micro-**
 224 **structures (μm), f solid fraction prior to oil impregnation. θ_a advancing contact angle ($^\circ$) and θ_r ,**
 225 **receding contact angle ($^\circ$) on slippery lubricant infused porous surfaces after impregnation.**

	Mn_{SLIPS}	mn_{SLIPS}	n_{SLIPS}	N_{SLIPS}
S_{RMS} (μm)	2.1 ± 0.5	1.4 ± 0.3	0.8 ± 0.1	0.6 ± 0.1
S_z (μm)	16.8	10.7	-	-
f	0.13	0.12	0.11	0.10
θ_a ($^\circ$)	$114^\circ \pm 2^\circ$	$117^\circ \pm 1^\circ$	$118^\circ \pm 2^\circ$	$118^\circ \pm 1^\circ$
θ_r ($^\circ$)	$111^\circ \pm 1^\circ$	$114^\circ \pm 1^\circ$	$115^\circ \pm 2^\circ$	$115^\circ \pm 1^\circ$

226 From the wettability characterisation presented above we stress here that the presence or
 227 absence of micro-structures underneath the infused lubricant does not influence considerably
 228 the macroscopic θ_a and θ_r and/or the contact angle hysteresis (CAH) defined as $CAH = \theta_r - \theta_a$.

229 After characterising the surface structure and wettability of our SLIPSSs, in order to fully
 230 describe the interactions between sessile droplet and our SLIPSSs, we further discuss on the
 231 interactions between water droplets, the lubricant and the surface. On one hand, to satisfy the
 232 stability of the SLIPSSs upon interaction with water, the immiscibility between the lubricant and
 233 water must be ensured, hence we make use of Krytox[®] GPL103 as per its earlier reported
 234 immiscibility in water [65]. On the other hand, a layer of lubricant may develop over the droplet,
 235 which is known as cloaking [37, 40, 65]. For moderate and high surface energy lubricant, the
 236 spreading coefficient is typically negative and hence the encapsulation of the droplet by the
 237 lubricant does not occur [37]. Whereas for a low surface tension lubricant and hence a positive
 238 spreading coefficient, the lubricant does typically cloak/encapsulate the droplet [37]. In the
 239 present cases, cloaking of the droplet by a thin lubricant film is expected [48, 57, 65]. The thin
 240 nature of the cloaking film in the order of tens of nanometres should in turn not influence
 241 considerably the theoretical heat transfer performance proposed here [2, 40].

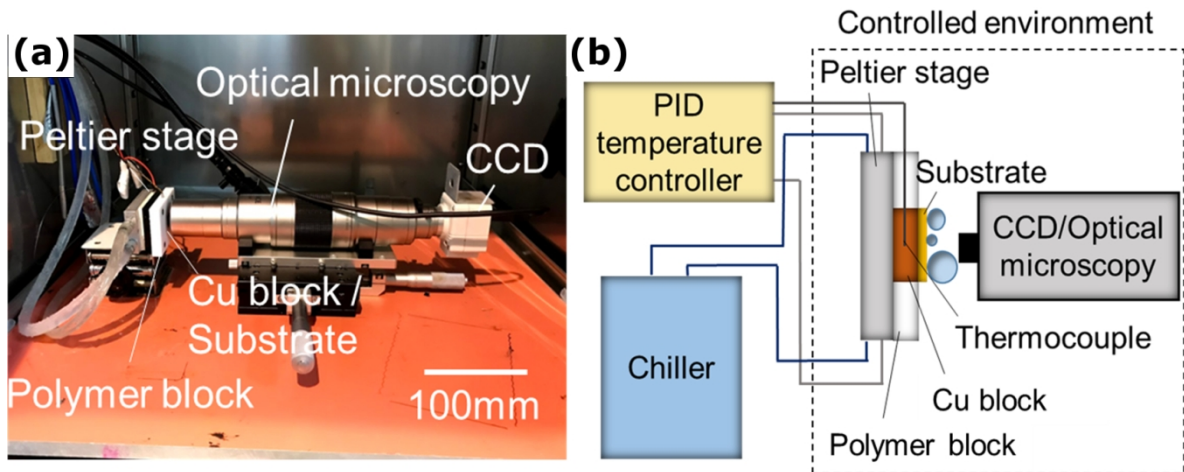
242

243 **Experimental apparatus and procedure**

244 All experimental observations were carried out in an environmental chamber PR-3KT from
245 ESPEC Corp. (Japan). Inside the environmental chamber, a custom-built Peltier stage,
246 connected to a PID controller and to a cooling bath both located outside the chamber, is placed
247 vertically. A custom-built copper block of the same area as the SLIPS samples ($10 \times 10 \text{ mm}^2$)
248 was inserted in a thermally insulating TEFLON block both with thicknesses of 10 mm and
249 attached to the Peltier stage to ensure 1 dimensional (1D) heat transfer between the Peltier stage
250 and the SLIPSs. A thermocouple was then set at the centre of the copper block few millimetres
251 below the SLIPS sample. Then, SLIPSs was attached to the copper block using double side
252 carbon tape. To ensure homogenous conditions within the chamber, prior to condensation
253 experimental observations, the temperature T_{amb} and the relative humidity RH of the ambient
254 air inside the chamber, i.e., in the presence of non-condensable gases, were set at $30 \text{ }^\circ\text{C} \pm 1 \text{ }^\circ\text{C}$
255 and at $90\% \pm 5\%$ respectively for 30 minutes. While the substrate temperature T_{sub} was set at
256 $35 \text{ }^\circ\text{C}$, which is above the water dew temperature so to avoid any condensation. Thereafter,
257 T_{sub} was lowered to $5 \text{ }^\circ\text{C}$, environmental chamber was turned off and experimental observations
258 were recorded. We note here that in spite of the environmental chamber being turned off to
259 avoid any vibration, the overall relative humidity was within $\pm 5\%$ for the entire duration of
260 the experiments. However, locally near the surface, the concentration of the water vapour may
261 be lower than that reported by the chamber. In addition, the use of a non-long working distance
262 lens for the optical microscopy observations may also shield the homogeneous diffusion of
263 water vapour towards the surface.

264 To allow for the acquisition of the experimental observations, a CCD camera Sentech STC-
265 MC152USB with a resolution of 1360×1024 pixels was utilised. On one hand, optical
266 microscopy experimental observations were acquired by making use of a Keyence high-
267 resolution optical microscopy zoom lens VH-Z500R with a field of view of $(590 \pm 5) \times (445 \pm$

268 5) μm^2 while a halogen lamp was used for coaxial illumination. On the other hand, a RICOH
 269 lens with a 30 mm spacing and a LED light were used for experimental observations at the
 270 macroscale with a field of view of $(5.0 \pm 0.1) \times (3.8 \pm 0.1) \text{ mm}^2$. A snapshot of the experimental
 271 setup inside of the chamber comprising: Peltier stage, optical microscope lens, CCD camera,
 272 x-y stage, tubing, cables and connections is found in Figure 3a; while detailed schematics of
 273 the complete setup is presented in Figure 3b. Snapshot including experimental setup and
 274 schematics for macroscopic experimental observations can be found in Figure SI2 in Section
 275 SI.2 in the accompanying SI.



276
 277 **Figure 3 – (a) Snapshot of the experimental setup inside the environmental chamber including**
 278 **Peltier stage, electrical connections, thermocouple connected to PID controller, water pipes**
 279 **connected to chiller, Copper-TEFLON block, SLIPS sample, CCD camera and optical**
 280 **microscope zoom lens VH-Z500R for microscopic observations. (b) Schematic of the complete**
 281 **experimental setup including environmental chamber, PID controller and chiller. Scale bar in**
 282 **Figure 3a is 100 mm. Snapshot and schematics of the experimental setup for macroscopic**
 283 **experimental observations equipped with the RICOH lens and 30 mm spacing can be found in**
 284 **Figure SI2 in Section SI.2 in the SI.**

285 Optical microscopy and macroscopic experimental observations were used to accurately
 286 determine the droplet size distribution, *i.e.*, droplet number density $N(r)$ [$\#/\text{mm}^3$] for the
 287 estimation of the theoretical heat transfer performance [2, 18, 66]. The droplet number density
 288 $N(r)$ [$\#/\text{mm}^3$] and the size of the droplets on our SLIPSs were extracted using Image-Pro

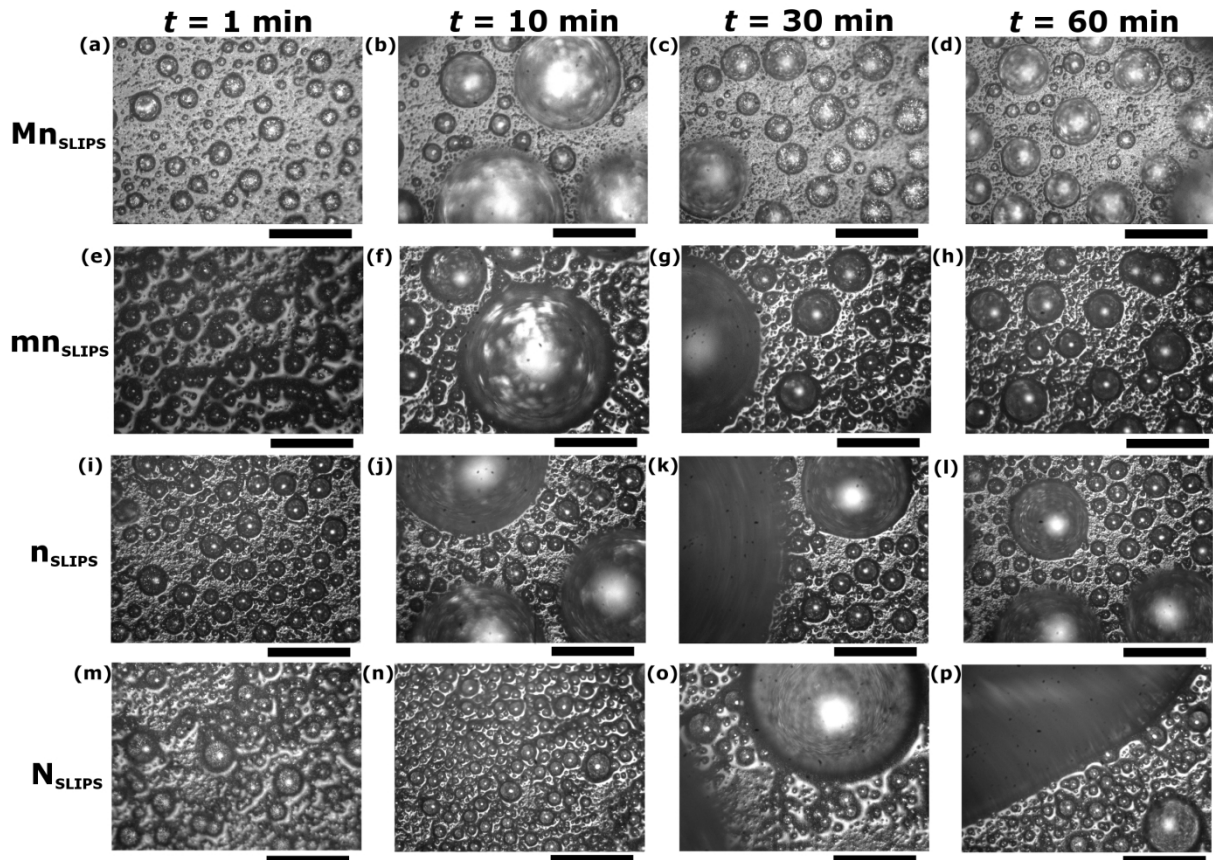
289 Plus[67] as follows. At different intervals of time, characteristic *instantaneous* snapshots were
290 analysed. From optical microscopy snapshots, the size and the number of droplets ranging
291 between 5 to 200 μm in radius were extracted by manually fitting circles to the contour of the
292 condensing droplets. In addition, to provide a more accurate characterisation of droplets with
293 sizes in the order of tens of micrometres and below, optical microscopy areas were analysed
294 applying a 4x magnification. On other hand, macroscopic observations were utilised to extract
295 the size and the number of droplets with radius ranging from 50 μm to 1 mm. Due to the
296 different droplet sizes and a single plane of view, the radius of the droplet is estimated with
297 $\pm 10\%$ accuracy. Data extracted using Image-Pro Plus was then imported to Origin and plotted.
298 More details on the procedure followed for the analysis of the droplet number density can be
299 found in Section SI.3 in the accompanying SI.

300

301 **Results**

302 **Condensation Dynamic Observations and Droplet Number Density Characterisation**

303 Characteristic optical microscopy snapshots during condensation on Mn_{SLIPS} , mn_{SLIPS} , n_{SLIPS} ,
 304 and N_{SLIPS} at different condensation times $t = 1, 10, 30$ and 60 minutes, with $t = 0$ minutes as
 305 the onset of nucleation, are presented in Figure 4:



306
 307 **Figure 4 – Characteristic optical microscopy snapshots of water condensation on (a-d) Mn_{SLIPS} ,**
 308 **(e-h) mn_{SLIPS} , (i-l) n_{SLIPS} and (m-p) N_{SLIPS} at 1 minute, 10 minutes, 30 minutes and 60 minutes with**
 309 **$t = 0$ seconds as the onset of nucleation. Scale bars are $200 \mu m$.**

310 When looking into optical microscopy experimental observations, a similar qualitative
 311 condensation behaviour on all SLIPSs is reported. Heterogeneous nucleation takes place evenly
 312 all over the surface on all four samples. The minimum radius for nucleation r_{min} can be
 313 estimated by making use of Kelvin's equation as: $r_{min} = \frac{2\gamma_{wa}T_{sat}}{\rho_w h_{fg} \Delta T}$, where γ_{wa} is the

314 surface tension water-air, T_{sat} is the saturation temperature of the vapour, ρ_w is the density of
315 the condensate, h_{fg} is the latent heat of gas to liquid phase-change and ΔT is the subcooling
316 condition imposed, i.e., difference of temperature between the vapour T_{sat} and the condenser
317 substrate T_{sub} [68-70]. Hence, for the same substrate temperature and environmental conditions
318 reported here, $r_{\text{min}} \approx 0.7$ nm independently of the SLIPS studied, which cannot be resolved
319 from optical microscopy observations. Then, as condensation develops, droplets grow via
320 direct condensation until they reach the effective transition radius, r_e , which is directly related
321 to the nucleation density N_s , before any coalescence takes place as: $r_e = 1/\sqrt{4N_s}$ [2, 16, 19,
322 71]. Thereafter, droplets grow via direct condensation and via coalescence with neighbouring
323 ones (Figure 4a,e,i,o). After several minutes from the onset of condensation, droplets in the
324 order of tens to hundreds of micrometres can be observed as in Figure 4b,f,j,o. As two or more
325 droplets coalesce, due to the low adhesion of the condensing droplets to the SLIPSs, the droplet
326 contact line is able to depin and retract. Then new area in the vicinity of the recent coalesced
327 droplet is available for re-nucleation and growth of small droplets. Eventually big droplets
328 disappear from the field of view as when comparing Figure 4b&c, Figure 4g&h and Figure 4
329 k-l. From optical microscopy (area field of view $590 \times 445 \mu\text{m}^2$) we cannot precisely state if
330 droplets are actually being removed by gravity, by sweeping or by coalescence with other
331 neighbouring droplets. Further observations making use of macroscopic experiments were
332 coupled with those at the micro-scale. An average shedding frequency of 4 ± 1 for Mn_{SLIPS} , 5
333 ± 1 for mn_{SLIPS} , 3 ± 1 for n_{SLIPS} and 3 ± 1 for N_{SLIPS} droplets per hour (major shedding events
334 averaged from 4 hours of experimental observations), demonstrated the cyclic nucleation,
335 growth, coalescence and shedding of the condensate occurring within the first 30 minutes.
336 Hence droplet number density analysis is here carried out and presented for the first 30 minutes.

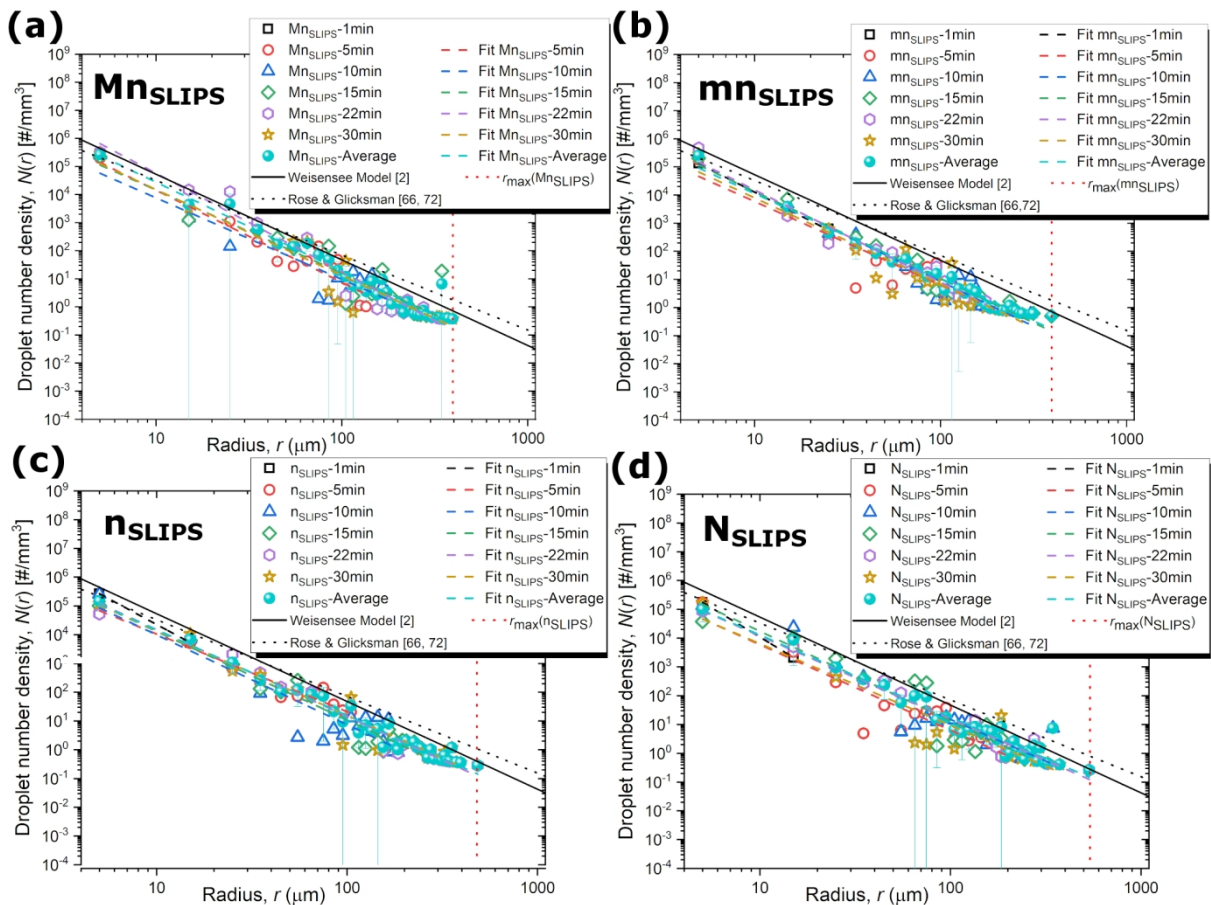
337 To evaluate the condensation performance on each of the structured surfaces studied, we
338 extract the droplet number density function of the droplet radius $N(r)$ [$\#/\text{mm}^3$] from optical

339 microscopy and from macroscopic experimental observations as $N(r) = \frac{N_{re}(r)/A}{r_{range}}$.

340 Where $N_{re}(r)$ is the droplet density or number of droplets of certain radius r , A is the area of
 341 observation equals to the optical microscopy or to the macroscopic field of view adopted during
 342 the experimental observations and r_{range} is the average droplet radius between the two extremes
 343 of the size range at which the droplet number density $N_{re}(r)$ was retrieved. $N(r) [\#/mm^3]$ relates
 344 then to the number and to the size of the droplets. The droplet number density $N(r) [\#/mm^3]$ is
 345 eventually used to estimate the theoretical heat transfer performance [2, 9, 18, 19].

346 Next, the droplet number density $N(r) [\#/mm^3]$ versus droplet radius $r [\mu m]$ is plotted in
 347 Figure 5 for Mn_{SLIPS} , mn_{SLIPS} , n_{SLIPS} , and N_{SLIPS} at $t = 1, 5, 10, 15, 22$ and 30 minutes along
 348 with their average over the presented times:

349



350

351 **Figure 5 – Droplet number density, $N(r) [\#/mm^3]$, versus droplet radius, $r [\mu m]$, extracted by**
 352 **Image-Pro Plus[67] for (a) Mn_{SLIPS} , (b) mn_{SLIPS} , (c) n_{SLIPS} , and (d) N_{SLIPS} at $t = 1$ (black squares),**

353 **5 (red circles), 10 (blue up-triangles) 15 (green rhomboids), 22 (purple hexagons), 30 (gold stars)**
 354 **minutes, and the averaged droplet number density (cyan spheres). Coloured dashed lines are**
 355 **included to illustrate the power law trends for the different condensation times and average one.**
 356 **In addition, droplet number density power-law fitting proposed by Weisensee *et al.* is included in**
 357 **black solid line [2] and correlation developed by Rose and Glicksman is included in black dotted**
 358 **line [66, 72]. In vertical red dotted lines, the maximum experimental radius, r_{\max} , obtained from**
 359 **macroscopic observations of droplet shedding is represented. For a more direct comparison**
 360 **between the different droplet number densities on the different SLIPs, the reader is referred to**
 361 **Figure 7b of the manuscript. Error bars represent the droplet number density standard deviation**
 362 **for the averaged case. Note error bars below x-axis as per the standard deviation in the same**
 363 **order of magnitude as the averaged values.**

364 From Figure 5, the droplet number density follows a similar qualitative behaviour regardless
 365 of the surface micro- and/or nano-structure underneath the lubricant and the condensing
 366 droplets. Reported trends on Mn_{SLIPs} , mn_{SLIPs} , n_{SLIPs} , and N_{SLIPs} are in qualitative agreement

367 with the model proposed by Rose and Glicksman where $N(r) = \frac{1}{3\pi r_e^2 \hat{r}} \left(\frac{r}{\hat{r}}\right)^{-2/3}$ [66, 72],

368 and the power-law fitting and average droplet density function included in the work of
 369 Weisensee *et al.*[2] (see Figure 5 and Figure 7b). Where $\hat{r} = r_{\max}/1.3$ and r_{\max} is calculated as:

370
$$r_{\max} = \left(\frac{6(\cos\theta_r - \cos\theta_a)\sin\theta_e \gamma_{\text{wa}}}{\pi(2 - 3\cos\theta_e + \cos\theta_e)\rho_l g} \right)^{0.5}$$
 with θ_e as the average

371 contact angle between the advancing and receding contact angles estimated as: $\theta_e = \cos^{-1}(0.5$
 372 $\cos\theta_a + 0.5\cos\theta_r)$.

373 We highlight here that neither the different micro-/nano-structures underneath the
 374 condensing droplets nor the different experimental conditions influenced qualitatively the
 375 intrinsic droplet number density, although some quantitative differences may arise from the
 376 different subcooling and environmental conditions[8, 66]. All trends follow: $N(r) = ar^{-b}$,
 377 where b represents the inclination of the slope and dictates how the droplet number density
 378 changes with droplet size, while a is a coefficient in the order of 10^7 [2]. From Figure 5 it can

379 also be extracted that at early stages of condensation, *i.e.*, $t = 1$ minute, experimental coefficient
380 b is greater than for developed condensation times with values ranging between 3.2 and 4.0.
381 This is due to the great number of small droplets with sizes in the order of tens of micrometres
382 experiencing their initial growth and to the absence of droplets with sizes above tens of
383 micrometres. For greater condensation times, *i.e.*, $t \geq 5$ minutes, the average and standard
384 deviation of the coefficient b can be quantitatively compared to those earlier reported in
385 literature, which are further discussed below [2, 72-74]. Table 2 includes the different a and b
386 coefficients extracted from experimental observations for $t = 5, 10, 15, 22$ and 30 minutes for
387 Mn_{SLIPS} , mn_{SLIPS} , n_{SLIPS} and N_{SLIPS} :

388 **Table 2 – Fitting coefficients a and b extracted from experimental observations at $t = 5, 10, 15,$
389 **22 and 30 minutes and averaged one, following the trend $N(r) = ar^{-b}$ for Mn_{SLIPS} , mn_{SLIPS} ,
390 n_{SLIPS} and N_{SLIPS} . Standard deviation for a and b coefficients are estimated as $\pm 1 \times 10^7$ and ± 0.16 .****

	Mn_{SLIPS}		mn_{SLIPS}		n_{SLIPS}		N_{SLIPS}	
	a	b	a	b	a	b	a	b
$t = 5$	2.73×10^7	3.28	5.51×10^6	2.97	5.27×10^6	2.7	5.51×10^6	2.97
$t = 10$	6.17×10^6	2.90	2.01×10^7	3.19	1.30×10^7	3.12	9.47×10^6	2.90
$t = 15$	1.33×10^7	2.96	1.75×10^7	3.11	1.54×10^7	3.08	2.22×10^7	3.10
$t = 22$	1.51×10^8	3.45	2.91×10^7	3.28	1.58×10^7	3.02	9.41×10^6	2.89
$t = 30$	1.73×10^7	3.06	9.35×10^6	3.07	1.27×10^7	2.96	4.45×10^6	2.84
Average	3.74×10^7	3.14	1.18×10^7	3.02	1.53×10^7	2.97	9.26×10^6	2.86

391

392 Coefficients b calculated for Mn_{SLIPS} , mn_{SLIPS} , n_{SLIPS} and N_{SLIPS} included in Table 2 are
393 within the standard deviation and in agreement with the work of Weisensee *et al.* where b
394 equals 3.05 [2]. The less inclined slope reported in the case of nano-structured n_{SLIPS} and N_{SLIPS}
395 is, on the other hand, attributed to the presence of greater number of big droplets over the
396 intervals of time studied. In the case of n_{SLIPS} and N_{SLIPS} , droplets seem to be less mobile due

397 to stronger pinning to the surface when compared to Mn_{SLIPS} and mn_{SLIPS} . The greater b
398 coefficients reported here (Table 2) when compared to the works of Tanaka, Watanabe *et al.*
399 and Tanasawa (reported values between 2.6 and 2.7) are attributed to the better mobility of the
400 droplets in the submillimetre range on SLIPSs when compared to smooth hydrophobic surfaces
401 with shedding sizes above a millimetre [73-75]. When looking into the a coefficient, average
402 values reported in Table 2 are found within the same order of magnitude to those reported by
403 Weisensee *et al.* equal 6×10^7 , although the magnitude of the our coefficients is 2 to 5 times
404 lower as a consequence of the lower subcooling, absence of artificial sweeping and/or the
405 different heat flux conditions imposed [2, 76]. On one hand, when looking into the
406 *instantaneous* droplet number densities reported at different condensation times ($t = 5, 10, 15,$
407 22 and 30 minutes), for droplets with sizes equal or smaller than $100 \mu\text{m}$, quantitative
408 differences are found when comparing the coefficient a reported in Table 2. More specifically,
409 by making use of $N(r) = ar^{-b}$ and for a given radius of $1 \mu\text{m}$, up to two orders of magnitude
410 difference in the droplet number density is put forward. On the other hand, the rather uniform
411 *instantaneous* droplet number densities reported in Figure 5 for droplets with sizes equal or
412 above $100 \mu\text{m}$, opposed to the large variability on the droplet number distribution after a
413 shedding event, is attributed to the field of view adopted during the macroscopic experimental
414 observations. The width of the observation area is approximately 5 mm while the size of the
415 shedding droplets is ca. 1 mm . Hence, after a shedding event, only a fraction of the surface
416 (between $1/5^{\text{th}}$ and $1/3^{\text{rd}}$) is actually refreshed while the droplet number density remains the
417 unaltered on the non-refreshed area, which in turn returns the observed rather homogeneous
418 distribution throughout the *instantaneous* snapshots. Variations in the droplet number density
419 at different condensation times were earlier pointed out by Rose and by other authors who
420 proposed the use of a *steady/average* droplet number density for the calculations of the
421 theoretical heat transfer in order to account for the variability of the droplet number density as

422 a consequence of the shedding/sweeping cycles [2, 66, 74, 77]. For a more direct comparison
423 between the different droplet number densities function of the SLIPSs, the reader can refer to
424 Figure 7b of the present manuscript. We note that the low magnification used in the
425 experiments did not allow for the accurate measurement of droplets with sizes below few
426 micrometres and/or for the observation of the self-propulsion of micro-droplets during
427 dropwise condensation on SLIPSs recently reported [78].

428 For the condensation times reported here, no appreciable shift of the DWC performance was
429 observed as a consequence of structure damage, peeling of the coating and/or oil depletion,
430 which in turn would induce the further pinning of the condensate and eventual FWC. In
431 addition, long-term condensation test was performed overnight for 11 hours on n_{SLIPS} showed
432 continuous DWC performance at any given condensation time under optical microscopy. As a
433 consequence of the optical microscopy technique utilized here, the extent of pinning and
434 whether there is a shift on the maximum experimental radius r_{max} could not be resolved, which
435 could be the scope for future research on the durability and stability of SLIPSs. To this extent,
436 we would like to remind the reader here that we recently demonstrated the feasibility of
437 operation of up to 192 hours within 16 experimental runs without appreciable change on the
438 overall heat transfer resistance of a two-phase closed thermosiphon paired with a
439 superhydrophilic evaporator and a SLIPS condenser. SLIPS condenser was fabricated and
440 impregnated following the very same procedure as the SLIPSs reported in this work [57].

441

442 **Steady State Heat Transfer through Condensing Droplets**

443 Next, we estimate the theoretical surface heat flux at the different condensation times on
444 each of our SLIPSs. The theoretical surface heat flux, q'' (kw/m²), can be calculated from
445 coupling the individual droplet heat transfer function of their radius, $q_d(r)$, to the droplet

446 number density $N(r)$ as: $q'' = \int q_d(r)N(r)dr$ [2, 71]. Since typically during dropwise
 447 condensation droplet growth takes place via direct condensation for small droplet with radius
 448 below the transition radius r_e ($r < r_e$) and via droplet coalescence for droplets with radius above
 449 r_e ($r > r_e$), the total heat flux for dropwise condensation without taking into account droplet
 450 shedding or sweeping is expressed as [19, 79]:

$$q'' = \int_{r_{\min}}^{r_e} q_d(r)n(r)dr + \int_{r_e}^{r_{\max}} q_d(r)N(r)dr \quad \text{Eq. 1}$$

451 where $n(r)$ and $N(r)$ are the droplet number density or droplet size distribution of droplets below
 452 and above the transition radius r_e , respectively. The transition radius r_e is calculated from the
 453 nucleation site density N_s obtained before the first coalescence event taking place typically
 454 before the first minute of the experimental observation as: $r_e = 1/\sqrt{4N_s}$ equals 5.4 μm , 5.7 μm ,
 455 5.0 μm and 5.1 μm on Mn_{SLIPS} , mn_{SLIPS} , n_{SLIPS} and N_{SLIPS} , respectively. r_e values are in
 456 agreement with those reported in Ref. 2 between 0.5 and 10 μm [2]. Last, r_{\max} and r_{\min} are
 457 defined as the maximum and minimum radius for droplet shedding and for heterogeneous
 458 nucleation to occur, respectively [8, 68, 70, 80].

459 On one hand, the droplet size distribution above the transition radius $N(r)$ can be extracted
 460 from Figure 5 or from the different coefficients reported in Table 2, while the droplet size
 461 distribution for droplets below the transition radius $n(r)$ can be estimated from the expressions
 462 proposed by Graham and Griffith [8], Tanaka [73], Kim and Kim [19], Miljkovic *et al.* [81],
 463 Wen *et al.* [71], Chavan *et al.*[18], and Alizadeh-Birjandi [82], amongst others. Nonetheless,
 464 in order to solely rely on our experimental data avoiding the use of empirical correlations, in
 465 this work we only make use of the $N(r)$ reported in Figure 5 for droplets bigger than r_e .

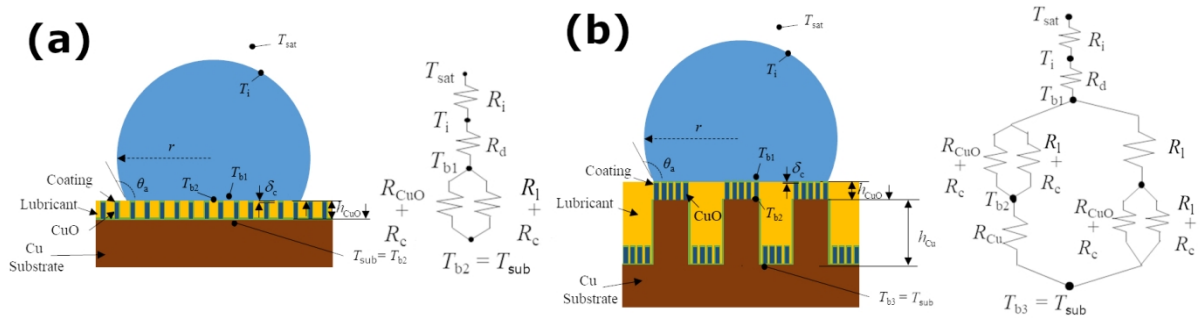
466 On the other hand, the heat transfer through a single droplet q_d can be calculated adopting a
 467 heat transfer thermal resistance based model for a droplet condensing on a hydrophobic surface
 468 developed by Kim and Kim [2, 9, 19]. On nano-structured SHSs though, q_d can then be

469 determined by making use of Kim and Kim's model adapted to account for the presence of
470 nano-structures as in the work of Miljkovic and Wang [9, 83]; while Weisensee *et al.* developed
471 a more appropriate model for nano-structured lubricant infused surfaces [2]. Nonetheless, the
472 presence of both micro-structures and nano-structures was not accounted for on earlier models,
473 which is one of the contributions of the present work. For the development of the heat transfer
474 resistance based model, the following assumptions/simplifications apply:

- 475 • the heat transfer resistance across the lubricant with thickness in the order of tens of
476 nanometres cloaking the droplet [40, 57] can be neglected as we are comparing droplets
477 with similar geometric configurations and the size of the droplets is at least two orders of
478 magnitude greater than the thickness of the film;
- 479 • the heat transfer resistance across the lubricant confined between the top of the nano-
480 structures and the condensing droplets is also neglected as the ternary configuration
481 surface-lubricant-water studied here behaves in the impregnated emerged state, *i.e.*, the
482 lubricant impregnates the structures but does not encapsulate their tops [37];
- 483 • the presence of a layer of Cu_2O earlier reported in the work of Enright *et al.* is also
484 neglected as all four SLIPs have been fabricated under similar conditions hence the
485 similar thickness of the Cu_2O layer and hence comparable heat transfer resistance [16];
- 486 • interfacial resistances between the droplet and the oil, the droplet and the solid surface,
487 and the oil and the solid surface can be neglected when compared to the other thermal
488 resistances, as assumed in the widely adopted thermal resistance based models [2, 9, 18,
489 19, 83].

490 After the above stated assumptions, schematics of the heat transfer resistance based model
491 in the absence and in the presence of micro-structures on our SLIPs can be found on Figure
492 6a and Figure 6b, respectively. The complete schematics of the heat transfer resistance-based

493 model through a single droplet and simplified one along with the relevant assumptions can be
 494 found in Section SI.4 in the accompanying SI as Figure SI4 and Figure SI5, respectively.



495
 496 **Figure 6 – Schematics of the heat transfer resistance based model adopted for the**
 497 **calculation of the thermal resistance thorough a single condensing droplet exerted by (a)**
 498 **the nano-structures, the hydrophobic coating, the lubricant and the droplet, and (b) the**
 499 **micro- and the nano-structures, the hydrophobic coating, the lubricant and the droplet.**

500 From Figure 6 it is clear that the thermal resistance through the bulk copper and the
 501 condensing droplets is then function of the presence or absence of micro-structures. The heat
 502 transfer resistance through an individual droplet making use of the heat transfer resistance base
 503 model presented in Figure 6 can be then calculated as in Eq. 2:

$$q_d = \frac{\Delta T}{R_{tot}} = \frac{\Delta T}{R_i + R_d + R_l + R_{m/n/c/l}} \quad \text{Eq. 2}$$

504 where R_{tot} is the total heat transfer resistance accounting for: R_i as the interfacial thermal
 505 resistance for condensation, R_d as the thermal resistance across the droplet, R_l as the thermal
 506 resistance across the lubricant and $R_{m/n/c/l}$ as the thermal resistance imposed by the micro- and
 507 the nano-structures, the hydrophobic coating underneath the lubricant and the lubricant. In the
 508 absence of micro-structures, $R_{m/n/c/l}$ is then replaced by $R_{n/c/l}$ where only the presence of nano-
 509 structures, the coating and the lubricant between the structures is accounted for as for earlier
 510 reported superhydrophobic surfaces [9, 16, 83]. ΔT is the degree of subcooling typically
 511 defined as the temperature between the vapour and the condenser surface $\Delta T = T_{sat} - T_{sub}$. ΔT

512 is calculated taking into account the Kelvin effect ΔT_c due to droplet the curvature r , as: $\Delta T =$
 513 $T_v - T_s - \Delta T_c$ with $\Delta T_c = \frac{2T_{sat}\gamma_{wa}}{h_{fg}r\rho_w}$ [18, 84].

514 The interfacial thermal resistance is calculated as: $R_i = \frac{1}{h_i 2\pi r^2 (1 - \cos\theta_a)}$ with h_i as the
 515 interfacial heat transfer coefficient $h_i = \frac{2\alpha}{(2-\alpha)\sqrt{2\pi R_g T_{sat}}} \frac{1}{T_{sat}} \frac{\rho_v h_{fg}^2}{T_{sat}}$, where α is the accommodation
 516 coefficient function of the condensation conditions and the amount of non-condensable gases
 517 [8, 9], R_g is the specific gas constant and ρ_v the water vapour specific density. All fluid and
 518 vapour properties were estimated at T_{sub} , whereas the accommodation coefficient is assumed
 519 as 0.04 as in the presence of condensable gases [2, 18]. The conduction thermal resistance
 520 across the droplet is estimated from the droplet size as: $R_d = \frac{\theta_a}{4\pi k_w r \sin\theta_a}$ where k_w is the
 521 water thermal resistance ($k_w = 0.57$ W/m/K). R_l is the heat transfer resistance imposed by the
 522 lubricant layer above the micro- and/or the nano-structures as: $R_l = \frac{\delta_l}{\pi r^2 k_l \sin^2\theta_a}$, where δ_o
 523 and k_o are the thickness and the thermal conductivity of the Krytox[®] lubricant, respectively,
 524 which is neglected as per the impregnated emerged state reported. The heat transfer resistance
 525 imposed by the lubricant in between the micro- and the nano-structures will be then accounted
 526 for in $R_{m/n/c/l}$ and in $R_{n/c/l}$.

527 On one hand, in the absence of micro-structures, the thermal resistance between the base of
 528 the droplet and the solid surface $R_{n/c/l}$ can be considered as a resistance in parallel across the
 529 nano-structures and the coating, and across the coating and the lubricant present within the
 530 nano-structures. $R_{n/c/l}$ is then calculated as:

$$R_{n/c/l} = \frac{1}{\pi r^2 k_c \sin^2\theta_a} \left(\frac{k_{CuO} f_n}{\delta_c k_{CuO} + h_{CuO} k_c} + \frac{k_l (1 - f_n)}{\delta_c k_l + h_{CuO} k_c} \right)^{-1} \quad \text{Eq. 3}$$

531 where k_c , k_{CuO} and k_l are the thermal conductivity of the hydrophobic coating ($k_c = 0.2$ W/m/K)
532 [16], the copper oxide ($k_{\text{CuO}} = 20$ W/m/K) [2] and the Krytox[®] GPL103 ($k_l = 0.09$ W/m/K) [2],
533 respectively. δ_c is the thickness of the hydrophobic coating ($\delta_c = 1$ nm)[16] and h_{CuO} is the
534 height of the nano-structures estimated from SEM and in agreement with Ref. 55 as $h_{\text{CuO}} = 300$
535 ± 20 nm [55]. While f_n is the solid fraction of nano-structures estimated from the Cassie-Baxter
536 equation (solid fraction values from Table 1). Then, by substituting the different heat transfer
537 resistances (i.e., the thermal resistance across the nano-structured SLIPS $R_{n/c/l}$, the droplet heat
538 transfer resistance R_d and the condensation interfacial heat transfer resistance R_i) into Eq. 2, the
539 theoretical heat transfer through a single condensing droplet and through the nano-structured
540 SLIPS, i.e., in the absence of micro-structures, $q_{d/n/c/l}$ can be obtained as in Eq. 4:

$$q_{d/n/c/l} = \frac{\pi r^2 (T_v - T_s - \Delta T_c)}{\frac{1}{h_i 2(1 - \cos \theta_a)} + \frac{r \theta_a}{4k_w \sin \theta_a} + \frac{1}{k_c \sin^2 \theta_a} \left(\frac{k_{\text{CuO}} f_n}{\delta_c k_{\text{CuO}} + h_{\text{CuO}} k_c} + \frac{k_l (1 - f_n)}{\delta_c k_l + h_{\text{CuO}} k_c} \right)^{-1}} \quad \text{Eq. 4}$$

541 On the other hand, in the presence of micro-structures the thermal resistance across the
542 micro- and the nano-structures from the bulk surface to the condensing droplets must be
543 considered as two paths in parallel as in Figure 6b. In the presence of micro-structures, for the
544 area fraction corresponding to the solid fraction of micro-structures φ_m , the thermal resistance
545 is exerted by the copper micro-structures and an additional resistance in parallel including the
546 nano-structures and the coating and the lubricant and the coating as for the nano-structured
547 case $R_{n/c/l}$, i.e., Figure 6a and Eq. 3. The other path results from the area of void fraction ($1 -$
548 φ_m), i.e., absence of micro-structures, where a parallel resistance as in the nano-structured case
549 including the nano-structures, the coating and the lubricant $R_{n/c/l}$ and the additional presence of
550 lubricant in between the micro-structures must be accounted for. Then, $R_{m/n/c/l}$ is estimated as:

$$R_{m/n/c/l} = \varphi_m (R_{\text{Cu}} + R_{n/c/l}) + (1 - \varphi_m) (R_l + R_{n/c/l}) \quad \text{Eq. 5}$$

551 where R_l is the resistance imposed by the lubricant impregnated between the micro-structures
 552 with thickness equivalent to the height of the micro-structures h_{Cu} (included as S_z in Table 1)
 553 as $R_l = h_{Cu}/\pi r^2 k_l \sin^2 \theta_a$, while R_{Cu} is the resistance imposed by the micro-structures as $R_{Cu} =$
 554 $h_{Cu}/\pi r^2 k_{Cu} \sin^2 \theta_a$. Then by substituting Eq. 3 and the different heat transfer resistances R_{Cu}
 555 and R_l into Eq. 5, the heat transfer resistance on a SLIPS in the presence of both micro- and
 556 nano-structures, the coating and the lubricant present in between the micro- and the nano-
 557 structures, $R_{m/n/c/l}$ can be rewritten as Eq. 6:

$$R_{m/n/c/l} = \varphi_m \left(\frac{h_{Cu}}{\pi r^2 k_{Cu} \sin^2 \theta_a} + \frac{1}{\pi r^2 k_c \sin^2 \theta_a} \left(\frac{k_{Cu} \delta_c f_n}{\delta_c k_{CuO} + h_{CuO} k_c} + \frac{k_l (1 - f_n)}{\delta_c k_l + h_{CuO} k_c} \right)^{-1} \right) + \quad \text{Eq. 6}$$

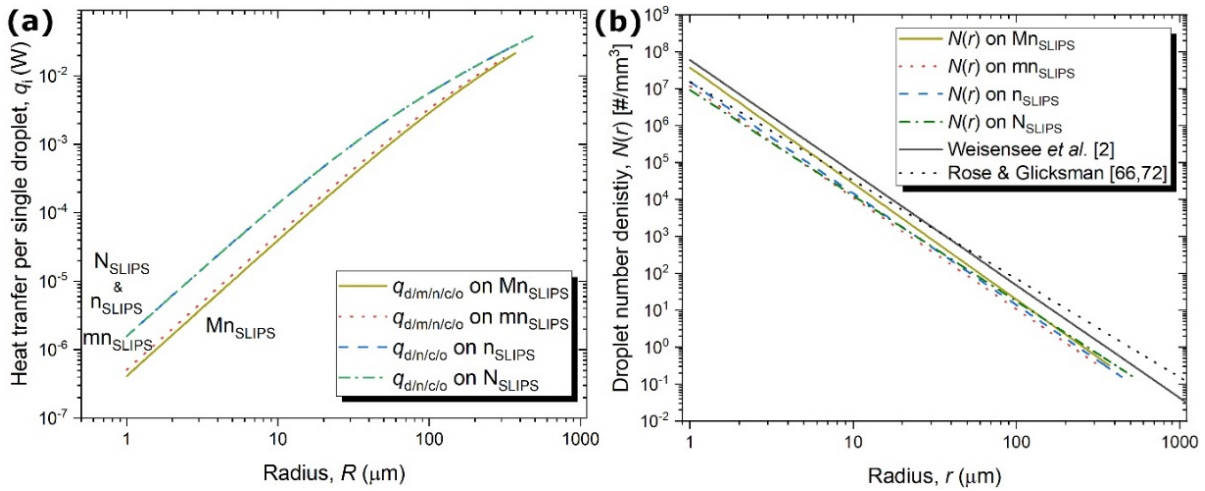
$$+ (1 - \varphi_m) \left(\frac{h_l}{\pi r^2 k_l \sin^2 \theta_a} + \frac{1}{\pi r^2 k_c \sin^2 \theta_a} \left(\frac{k_{Cu} \delta_c f_n}{\delta_c k_{CuO} + h_{CuO} k_c} + \frac{k_l (1 - f_n)}{\delta_c k_l + h_{CuO} k_c} \right)^{-1} \right)$$

558 Next, by substituting $R_{m/n/c/l}$ (Eq. 6) and the other heat transfer resistances, i.e., interfacial heat
 559 transfer resistance R_i and the heat transfer resistance through a condensing droplet R_d , into Eq.
 560 2, the theoretical heat transfer across a single droplet and across the micro-/nano-structured
 561 SLIPS $q_{d/m/n/c/l}$ adopts the form of Eq. 7:

$$q_{d/m/n/c/l} = \frac{\pi r^2 (T_v - T_s - \Delta T_c)}{\frac{1}{h_i^2 (1 - \cos \theta_a)} + \frac{r \theta_a}{4 k_w \sin \theta_a} + \left[\varphi_m \left(\frac{h_{Cu}}{\pi r^2 k_{Cu} \sin^2 \theta_a} + \frac{1}{\pi r^2 k_c \sin^2 \theta_a} \left(\frac{k_{Cu} \delta_c f_n}{\delta_c k_{CuO} + h_{CuO} k_c} + \frac{k_l (1 - f_n)}{\delta_c k_l + h_{CuO} k_c} \right)^{-1} \right) + \right. \quad \text{Eq. 7}$$

$$\left. + (1 - \varphi_m) \left(\frac{h_l}{\pi r^2 k_l \sin^2 \theta_a} + \frac{1}{\pi r^2 k_c \sin^2 \theta_a} \left(\frac{k_{Cu} \delta_c f_n}{\delta_c k_{CuO} + h_{CuO} k_c} + \frac{k_l (1 - f_n)}{\delta_c k_l + h_{CuO} k_c} \right)^{-1} \right) \right]}$$

562 Next, Figure 7a includes the different heat transfer through individual condensing droplets
 563 including the nano-structured surface and the oil for n_{SLIPS} and N_{SLIPS} as $q_{d/n/c/l}$; and through
 564 individual condensing droplets, the micro-/nano-structures and the oil on Mn_{SLIPS} and mn_{SLIPS}
 565 surfaces as $q_{d/m/n/c/l}$, which are calculated by making use of Eq. 4 and Eq. 7, respectively. In
 566 addition, Figure 7b includes the droplet number density averaged for the different condensation
 567 times analysed ($t = 5, 10, 15, 22$ and 30 minutes) for Mn_{SLIPS} , mn_{SLIPS} , n_{SLIPS} and N_{SLIPS} :



569

570 **Figure 7 – (a) Theoretical heat transfer through single condensing droplets, q_i (W), versus droplet**
 571 **radius, r (μm), and (b) average droplet number density $N(r)$ [$\#/\text{mm}^3$] versus droplet radius, r (μm),**
 572 **on Mn_{SLIPS} (gold solid line), mn_{SLIPS} (red dotted line), n_{SLIPS} (blue dashed line), and N_{SLIPS} (green**
 573 **dashed dotted line). Droplet number density power-law fitting proposed by Weisensee *et al.* is**
 574 **included in black solid line [2] and correlation developed by Rose and Glicksman is included in**
 575 **black dotted line [66, 72].**

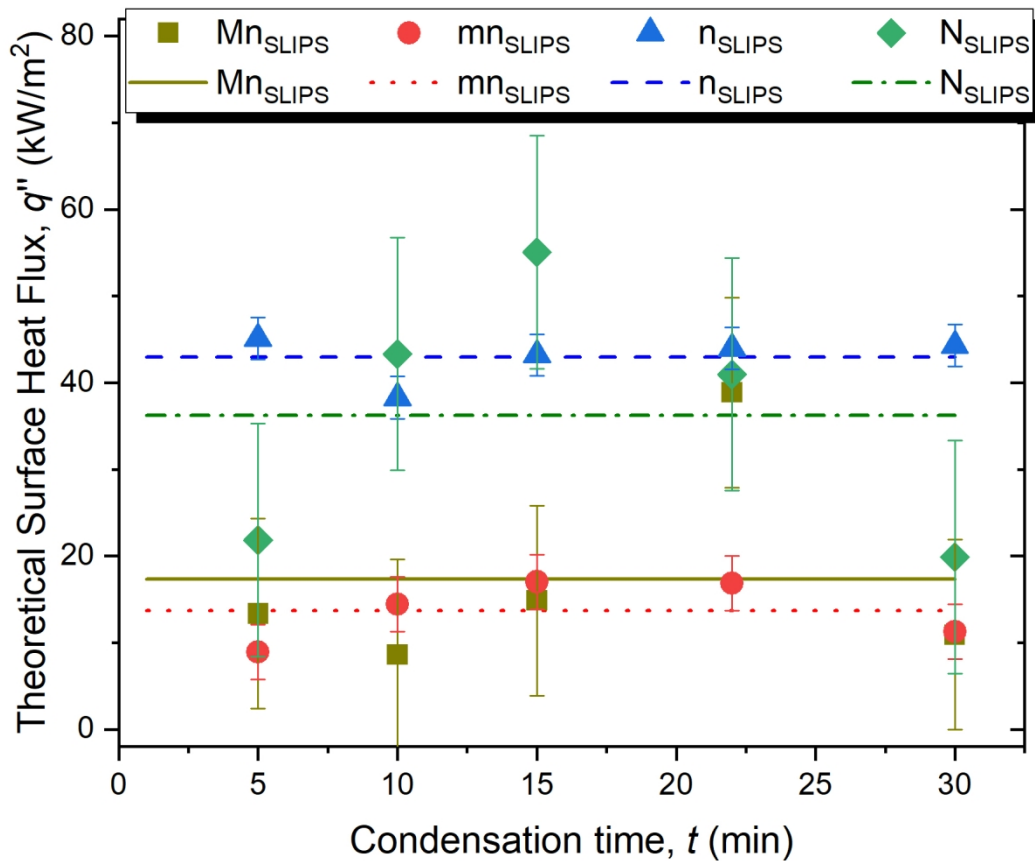
576 From Figure 7a, the different heat transfer through individual droplets function of the SLIPS
 577 underneath is presented. Clear differences when comparing the nano-structured n_{SLIPS} and
 578 N_{SLIPS} to the micro-/nano-structured Mn_{SLIPS} and mn_{SLIPS} are evident as a consequence of the
 579 greater heat transfer resistance imposed mainly by the lubricant present in between the micro-
 580 structures. Up to 50% greater heat transfer through individual droplets with sizes between 1
 581 and few tens of micrometres (for droplets with sizes in the same order of magnitude or below
 582 to that of the micro-structures) is put forward on solely nano-structured n_{SLIPS} and N_{SLIPS} when
 583 compared to hierarchical ones Mn_{SLIPS} and mn_{SLIPS} . It is only when the size of the condensing
 584 droplets becomes one order of magnitude greater than that of the micro-structures when the
 585 heat transfer through single condensing droplets approaches that on nano-structured one as the
 586 thermal resistance through the condensing droplets becomes dominant when compared to the
 587 substrate thermal resistance. When comparing the two hierarchical micro-/nano-structured
 588 SLIPSs, lower heat transfer values are reported for Mn_{SLIPS} due to the greater size of the micro-

589 structures (see S_z in Table 1) and hence greater thickness of the lubricant in between the
590 structures hindering the heat transfer. When comparing the nano-structured SLIPS n_{SLIPS} and
591 N_{SLIPS} no appreciable quantitative differences are observed as the structural parameters were
592 similar, i.e., in the same orders of magnitude, despite of the different shape and geometry of
593 the nano-features. Similar discussion applies if considering the heat transfer through the solid
594 surface structure negligible when compared to the other thermal resistances.

595 The greater heat transfer through single droplets on n_{SLIPS} and N_{SLIPS} will presumably
596 provide better heat transfer performance given that there are no major appreciable shifts on the
597 droplet number density or on the droplet size distribution when compared to Mn_{SLIPS} and
598 mn_{SLIPS} . The droplet number density may vary as a consequence of the different interactions
599 between the condensate and the different structured SLIPSs shifting the trends towards smaller
600 or bigger sizes of the condensing droplets depending on their ability for droplet shedding [56].
601 When looking into the droplet number density reported in Figure 7b no major qualitative
602 differences are found when comparing the averaged trends for all SLIPSs studied. It is noted
603 though that up to 50% greater number of droplets for droplet sizes between 1 and 10 μm on
604 hierarchical Mn_{SLIPS} when compared to mn_{SLIPS} , n_{SLIPS} and N_{SLIPS} , presumably due to the better
605 droplet shedding performance of Mn_{SLIPS} . We stress here on the reasonable qualitative and
606 quantitative (within the same orders of magnitude) agreement on the droplet number
607 distribution when comparing this work to Weisensee *et al.*, see Figure 7 [2].

608 Last, to obtain the theoretical surface heat flux q'' , we couple the theoretical heat transfer
609 through individual condensing droplets in the presence ($q_{\text{d/m/n/c/l}}$) and absence of micro-
610 structures ($q_{\text{d/n/c/l}}$) reported in Figure 7a to the experimental droplet number density $N(r)$
611 reported in Figure 5 for droplets above the transition radius r_e at different intervals of time t on
612 the different SLIPSs studied. Figure 8 provides the average theoretical surface heat flux q''
613 calculated from the averaged droplet size distribution reported in Figure 5 and the theoretical

614 surface heat flux at specific condensation times making use of their *instantaneous* droplet size
 615 distribution at $t = 5, 10, 15, 22$ and 30 minutes also included in Figure 5. By representing the
 616 surface heat flux at different condensation times rather than the averaged one, the cyclic
 617 dynamic condensation heat transfer when making use of instantaneous droplet number
 618 densities for Mn_{SLIPS} , mn_{SLIPS} , n_{SLIPS} , and N_{SLIPS} is captured. Moreover, we would like to
 619 highlight here that the theoretical surface heat flux reported in Figure 8 might be overestimated
 620 as per the presumably lower concentration and temperature of the water vapour near the
 621 condensing surface when compared to the conditions assumed. Local depletion of the water
 622 vapour concentration near surfaces as per the experimental conditions adopted.



623
 624 **Figure 8 – Theoretical surface heat flux, q'' (kW/m²), versus time, t (minutes), on Mn_{SLIPS}**
 625 **(squares), mn_{SLIPS} (circles), n_{SLIPS} (up-triangles), and N_{SLIPS} (rhomboids), at $t = 5, 10, 15, 22$ and**
 626 **30 minutes. Horizontal lines indicate the average theoretical surface heat flux, q'' (kW/m²),**
 627 **estimated from the average droplet number density reported in Figure 5 on Mn_{SLIPS} (solid line),**
 628 **mn_{SLIPS} (dotted line), n_{SLIPS} (dashed line) and N_{SLIPS} (dashed-dotted line). Error bars presented**

629 **have been calculated as the standard deviation of the different *instantaneous* theoretical heat**
630 **surface heat flux for $t = 5, 10, 15, 22$ and 30 minutes for each SLIPs.**

631 From Figure 8, the high and homogeneous theoretical surface heat flux in the order of tens
632 of kW/m^2 reported on the different SLIPs is owed to the low adhesion of the droplets to the
633 surface easing the continuous nucleation, growth and self-removal of the condensate in a
634 continuous DWC manner[6, 22, 66]. When comparing the different SLIPs, a 100% greater
635 overall theoretical surface heat flux is reported in the absence of micro-structures, i.e., n_{SLIPs}
636 and N_{SLIPs} , as a consequence of the reported 50% greater heat transfer through individual
637 condensing droplets with sizes of tens of micrometres and smaller reported in Figure 7a. The
638 presence of micro-structures exerts an additional heat transfer resistance through the micro-
639 structures and the lubricant on Mn_{SLIPs} and mn_{SLIPs} when compared to nano-structured n_{SLIPs}
640 and N_{SLIPs} , i.e., $R_{m/n/c/l} > R_{n/c/l}$; hence the lower theoretical surface heat flux reported on Mn_{SLIPs}
641 and mn_{SLIPs} . Theoretical surface heat flux values reported here are found within 10 kW/m^2 to
642 60 kW/m^2 , which are in the same range to those experimentally reported in the literature on
643 SHSs[11, 68] and on SLIPs[47] between 10 kW/m^2 and 200 kW/m^2 . The wide range of surface
644 heat flux arises from the different thermal resistance of the substrate, type of fluid, presence or
645 absence of non-condensable gases and/or subcooling conditions.

646 On a different note, the theoretical surface heat flux is also function of the droplet number
647 density, which in turn shifts depending on the ability of the surface to shed the condensate. In
648 the present case, the droplet size distribution for the hierarchical Mn_{SLIPs} is shifted towards
649 greater number of small sized droplets while the droplet number density is also constrained to
650 smaller droplet sizes as it was represented in Figure 5 and further summarized in Figure 7b.
651 Despite the 50% greater droplet number density found for droplet sizes between $1 \mu\text{m}$ and 10
652 μm on hierarchical Mn_{SLIPs} (Figure 7b), the additional heat transfer resistance imposed by the
653 micro-structures and the lubricant limits the heat transfer through individual droplets $q_{d/m/n/c/l}$

654 when compared to nano-structured n_{SLIPS} and N_{SLIPS} , i.e., $q_{d/m/n/c/l} < q_{d/n/c/l}$. As a consequence,
655 the heat transfer performance on hierarchical SLIPs is lower than that of nano-structured ones.
656 Last, we would like to highlight the cyclic oscillatory nature of the heat transfer values reported
657 in Figure 8 for each of the SLIPs studied. Theoretical heat transfer values in Figure 8 are
658 sensitive to the droplet number density $N(r)$ as per the different droplet number density versus
659 time reported in Figure 5 and Table 2.

660

661 **Conclusions**

662 An experimental investigation on the condensation performance of hierarchical micro- and
663 nano- and on nano-structured slippery lubricant infused porous surfaces (SLIPSs) has been
664 carried out. Two hierarchical micro-/nano-structured SLIPSs varying in the size and density of
665 the micro-structures and two nano-structured ones have been fabricated and observed under
666 optical microscopy and at the macroscale during condensation phase-change. From
667 experimental observations the average droplet number density and the droplet number density
668 at different condensation times ($t = 1, 5, 10, 15, 22$ and 30 minutes) have been extracted and
669 plotted versus droplet size. Different droplet number density and different maximum droplet
670 radius are reported depending on the SLIPSs and the condensation times studied. Up to 50%
671 greater droplet number density is reported on the hierarchical M_{SLIPS} for droplets sizes
672 between 1 and 10 micrometres, which is owed to the ability of this hierarchical surface to shed
673 the condensate shifting the droplet number density towards smaller sizes allowing for a greater
674 number of condensing droplets. Moreover, the transient nature of the droplet number density
675 is pointed out as one of the additional contribution of this work. Furthermore, resistance based
676 model earlier proposed for nano-structured superhydrophobic and lubricant infused surfaces is
677 revisited to account for the heat transfer through individual droplets in the presence of micro-
678 structures and nano-structures and the lubricant. A 50% greater heat transfer is achieved
679 through individual droplets in the absence of micro-structures when compared to hierarchical
680 SLIPSs caused by the absence of the additional thermal resistance imposed by the micro-
681 structures and the lubricant. Then, by coupling the heat transfer through individual droplets to
682 the droplet number density, the overall surface heat flux and the heat flux at different
683 condensation times is estimated. Up to 100% greater overall heat transfer performance is
684 estimated on nano-structured SLIPS (n_{SLIPS} and N_{SLIPS}) when compared to hierarchical ones
685 (M_{SLIPS} and m_{SLIPS}). Findings presented here are of importance for the optimisation and
686 characterisation of SLIPS for condensation heat transfer and other related applications.

687 **Acknowledgments**

688 D.O and Y.T. acknowledge the support received from the International Institute for Carbon-
689 Neutral Energy Research (WPI-I²CNER) and the Ministry of Education, Culture, Sports,
690 Science and Technology, Japan (MEXT). D.O. greatly acknowledges the support received by
691 the Japanese Society for the Promotion of Science (JSPS) KAKENHI, Japan (Grant No.
692 JP18K13703 and). P.Z. and F.Y.L. acknowledge the support of the National Natural Science
693 Foundation of China (Contract No. 51976117). F.Y.L. acknowledges the Natural Science
694 Foundation of Shanghai, China (Contract No. 19ZR1401700). The authors acknowledge Dr.
695 Sumitomo Hidaka from Kyushu University for his help and assistance on the experimental
696 setup. The authors acknowledge Professor Aleksandr N. Pavlenko (chair) and Dr. Anton
697 Surtaev (scientific secretary), organisers of the 5th International Workshop on Heat-Mass
698 Transfer Advances for Energy Conservation and Pollution Control held in Novosibirsk Russia,
699 for the hospitality, successful organisation and the invitation to submit this work as special
700 issue in Applied Thermal Engineering.

701

702 **Notes**

703 The authors declare no competing financial interests.

704

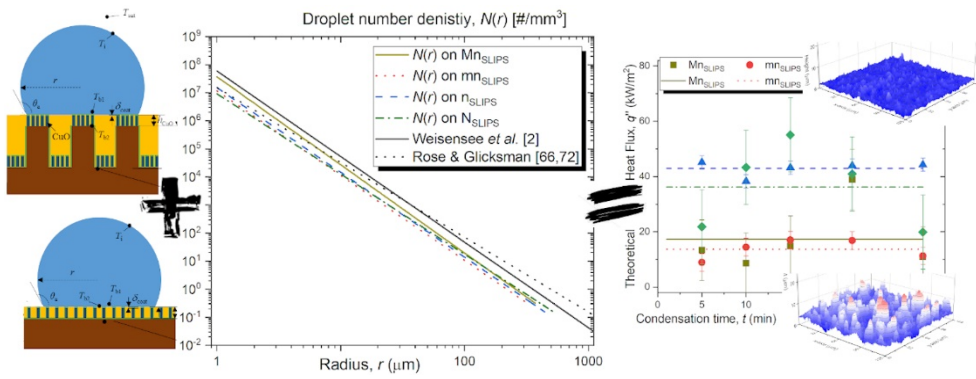
705

706

707

708

709 **Graphical Abstract**



710

711

712 References

- 713 [1] J.M. Beér, High efficiency electric power generation: The environmental role, *Progress in Energy*
714 and *Combustion Science*, 33 (2007) 107-134.
- 715 [2] P.B. Weisensee, Y. Wang, Q. Hongliang, D. Schultz, W.P. King, N. Miljkovic, Condensate droplet
716 size distribution on lubricant-infused surfaces, *International Journal of Heat and Mass Transfer*, 109
717 (2017) 187-199.
- 718 [3] E.J. Le Fevre, J.W. Rose, An experimental study of heat transfer by dropwise condensation,
719 *International Journal of Heat and Mass Transfer*, 8 (1965) 1117-1133.
- 720 [4] H.-Y. Kim, H.J. Lee, B.H. Kang, Sliding of Liquid Drops Down an Inclined Solid Surface, *Journal of*
721 *Colloid and Interface Science*, 247 (2002) 372-380.
- 722 [5] S. Vemuri, K.J. Kim, An experimental and theoretical study on the concept of dropwise
723 condensation, *International Journal of Heat and Mass Transfer*, 49 (2006) 649-657.
- 724 [6] D. Attinger, C. Frankiewicz, A.R. Betz, T.M. Schutzius, R. Ganguly, A. Das, C.-J. Kim, C.M.
725 Megaridis, *Surface engineering for phase change heat transfer: A review*, *MRS Energy &*
726 *Sustainability*, 1 (2014).
- 727 [7] A. Umur, P. Griffith, Mechanism of Dropwise Condensation, *Journal of Heat Transfer*, 87 (1965)
728 275-282.
- 729 [8] C. Graham, P. Griffith, Drop size distributions and heat transfer in dropwise condensation,
730 *International Journal of Heat and Mass Transfer*, 16 (1973) 337-346.
- 731 [9] N. Miljkovic, R. Enright, E.N. Wang, Effect of Droplet Morphology on Growth Dynamics and Heat
732 Transfer during Condensation on Superhydrophobic Nanostructured Surfaces, *ACS Nano*, 6 (2012)
733 1776-1785.
- 734 [10] C.-H. Chen, Q. Cai, C. Tsai, C.-L. Chen, G. Xiong, Y. Yu, Z. Ren, Dropwise condensation on
735 superhydrophobic surfaces with two-tier roughness, *Applied Physics Letters*, 90 (2007) 173108.
- 736 [11] N. Miljkovic, R. Enright, Y. Nam, K. Lopez, N. Dou, J. Sack, E.N. Wang, Jumping-Droplet-Enhanced
737 Condensation on Scalable Superhydrophobic Nanostructured Surfaces, *Nano Letters*, 13 (2013) 179-
738 187.
- 739 [12] R. Parin, A. Martucci, M. Sturaro, S. Bortolin, M. Bersani, F. Carraro, D. Del Col, Nano-structured
740 aluminum surfaces for dropwise condensation, *Surface and Coatings Technology*, 348 (2018) 1-12.
- 741 [13] M.D. Mulroe, B.R. Srijanto, S.F. Ahmadi, C.P. Collier, J.B. Boreyko, Tuning Superhydrophobic
742 Nanostructures To Enhance Jumping-Droplet Condensation, *ACS Nano*, 11 (2017) 8499-8510.
- 743 [14] E. Ölçeroğlu, M. McCarthy, Self-Organization of Microscale Condensate for Delayed Flooding of
744 Nanostructured Superhydrophobic Surfaces, *ACS Applied Materials & Interfaces*, 8 (2016) 5729-
745 5736.
- 746 [15] J.B. Boreyko, C.-H. Chen, Self-Propelled Dropwise Condensate on Superhydrophobic Surfaces,
747 *Physical Review Letters*, 103 (2009) 184501.
- 748 [16] R. Enright, N. Miljkovic, N. Dou, Y. Nam, E.N. Wang, Condensation on Superhydrophobic Copper
749 Oxide Nanostructures, *Journal of Heat Transfer*, 135 (2013) 091304-091304-091312.
- 750 [17] R. Parin, M. Sturaro, S. Bortolin, A. Martucci, D. Del Col, Heat transfer during dropwise
751 condensation of steam over a mirror polished sol-gel coated aluminum substrate, *International*
752 *Journal of Thermal Sciences*, 144 (2019) 93-106.
- 753 [18] S. Chavan, H. Cha, D. Orejon, K. Nawaz, N. Singla, Y.F. Yeung, D. Park, D.H. Kang, Y. Chang, Y.
754 Takata, N. Miljkovic, Heat Transfer through a Condensate Droplet on Hydrophobic and
755 Nanostructured Superhydrophobic Surfaces, *Langmuir*, 32 (2016) 7774-7787.
- 756 [19] S. Kim, K.J. Kim, Dropwise Condensation Modeling Suitable for Superhydrophobic Surfaces,
757 *Journal of Heat Transfer*, 133 (2011) 081502-081502-081508.
- 758 [20] A. Lafuma, D. Quéré, Superhydrophobic states, *Nature Materials*, 2 (2003) 457.
- 759 [21] C. Neinhuis, W. Barthlott, Characterization and Distribution of Water-repellent, Self-cleaning
760 Plant Surfaces, *Annals of Botany*, 79 (1997) 667-677.

761 [22] D. Orejon, O. Shardt, N.S.K. Gunda, T. Ikuta, K. Takahashi, Y. Takata, S.K. Mitra, Simultaneous
762 dropwise and filmwise condensation on hydrophilic microstructured surfaces, *International Journal*
763 *of Heat and Mass Transfer*, 114 (2017) 187-197.

764 [23] D. Orejon, O. Shardt, P.R. Waghmare, N.S. Kumar Gunda, Y. Takata, S.K. Mitra, Droplet migration
765 during condensation on chemically patterned micropillars, *RSC Advances*, 6 (2016) 36698-36704.

766 [24] P.S. Mahapatra, A. Ghosh, R. Ganguly, C.M. Megaridis, Key design and operating parameters for
767 enhancing dropwise condensation through wettability patterning, *International Journal of Heat and*
768 *Mass Transfer*, 92 (2016) 877-883.

769 [25] E. Ölçeroğlu, C.-Y. Hsieh, K.K.S. Lau, M. McCarthy, Thin Film Condensation Supported on
770 Ambiphilic Microstructures, *Journal of Heat Transfer*, 139 (2017) 020910-020910-020911.

771 [26] R.L. Winter, M. McCarthy, Dewetting from Amphiphilic Minichannel Surfaces during
772 Condensation, *ACS Applied Materials & Interfaces*, (2020).

773 [27] J. Oh, R. Zhang, P.P. Shetty, J.A. Krogstad, P.V. Braun, N. Miljkovic, Thin Film Condensation on
774 Nanostructured Surfaces, *Advanced Functional Materials*, 1707000-n/a.

775 [28] Y. Shang, Y. Hou, M. Yu, S. Yao, Modeling and optimization of condensation heat transfer at
776 biphilic interface, *International Journal of Heat and Mass Transfer*, 122 (2018) 117-127.

777 [29] Y. Hou, M. Yu, X. Chen, Z. Wang, S. Yao, Recurrent Filmwise and Dropwise Condensation on a
778 Beetle Mimetic Surface, *ACS Nano*, 9 (2015) 71-81.

779 [30] D. Orejon, A. Askounis, Y. Takata, D. Attinger, Dropwise Condensation on Multiscale Bioinspired
780 Metallic Surfaces with Nanofeatures, *ACS Applied Materials & Interfaces*, 11 (2019) 24735-24750.

781 [31] X. Yan, Z. Huang, S. Sett, J. Oh, H. Cha, L. Li, L. Feng, Y. Wu, C. Zhao, D. Orejon, F. Chen, N.
782 Miljkovic, Atmosphere-Mediated Superhydrophobicity of Rationally Designed Micro/Nanostructured
783 Surfaces, *ACS Nano*, 13 (2019) 4160-4173.

784 [32] D.J. Preston, N. Miljkovic, J. Sack, R. Enright, J. Queeney, E.N. Wang, Effect of hydrocarbon
785 adsorption on the wettability of rare earth oxide ceramics, *Applied Physics Letters*, 105 (2014)
786 011601.

787 [33] L.B. Boinovich, A.M. Emelyanenko, A.S. Pashinin, C.H. Lee, J. Drelich, Y.K. Yap, Origins of
788 Thermodynamically Stable Superhydrophobicity of Boron Nitride Nanotubes Coatings, *Langmuir*, 28
789 (2012) 1206-1216.

790 [34] H.F. Bohn, W. Federle, Insect aquaplaning: *Nepenthes* pitcher plants capture prey with the
791 peristome, a fully wettable water-lubricated anisotropic surface, *Proceedings of the National*
792 *Academy of Sciences of the United States of America*, 101 (2004) 14138-14143.

793 [35] T.-S. Wong, S.H. Kang, S.K.Y. Tang, E.J. Smythe, B.D. Hatton, A. Grinthal, J. Aizenberg, Bioinspired
794 self-repairing slippery surfaces with pressure-stable omniphobicity, *Nature*, 477 (2011) 443-447.

795 [36] T.-S. Wong, T. Sun, L. Feng, J. Aizenberg, Interfacial materials with special wettability, *MRS*
796 *Bulletin*, 38 (2013) 366-371.

797 [37] J.D. Smith, R. Dhiman, S. Anand, E. Reza-Garduno, R.E. Cohen, G.H. McKinley, K.K. Varanasi,
798 Droplet mobility on lubricant-impregnated surfaces, *Soft Matter*, 9 (2013) 1772-1780.

799 [38] C. Hao, J. Li, Y. Liu, X. Zhou, Y. Liu, R. Liu, L. Che, W. Zhou, D. Sun, L. Li, L. Xu, Z. Wang,
800 Superhydrophobic-like tunable droplet bouncing on slippery liquid interfaces, *Nature*
801 *Communications*, 6 (2015) 7986.

802 [39] K. Rykaczewski, A.T. Paxson, M. Staymates, M.L. Walker, X. Sun, S. Anand, S. Srinivasan, G.H.
803 McKinley, J. Chinn, J.H.J. Scott, K.K. Varanasi, Dropwise Condensation of Low Surface Tension Fluids
804 on Omniphobic Surfaces, *Scientific Reports*, 4 (2014) 4158.

805 [40] J.B. Boreyko, G. Polizos, P.G. Datskos, S.A. Sarles, C.P. Collier, Air-stable droplet interface
806 bilayers on oil-infused surfaces, *Proceedings of the National Academy of Sciences*, 111 (2014) 7588-
807 7593.

808 [41] S. Nishimoto, B. Bhushan, Bioinspired self-cleaning surfaces with superhydrophobicity,
809 superoleophobicity, and superhydrophilicity, *RSC Advances*, 3 (2013) 671-690.

810 [42] B.R. Solomon, K.S. Khalil, K.K. Varanasi, Drag Reduction using Lubricant-Impregnated Surfaces in
811 Viscous Laminar Flow, *Langmuir*, 30 (2014) 10970-10976.

812 [43] P. Kim, T.-S. Wong, J. Alvarenga, M.J. Kreder, W.E. Adorno-Martinez, J. Aizenberg, Liquid-Infused
813 Nanostructured Surfaces with Extreme Anti-Ice and Anti-Frost Performance, *ACS Nano*, 6 (2012)
814 6569-6577.

815 [44] K.-C. Park, P. Kim, A. Grinthal, N. He, D. Fox, J.C. Weaver, J. Aizenberg, Condensation on slippery
816 asymmetric bumps, *Nature*, advance online publication (2016).

817 [45] R. Xiao, N. Miljkovic, R. Enright, E.N. Wang, Immersion Condensation on Oil-Infused
818 Heterogeneous Surfaces for Enhanced Heat Transfer, *Scientific Reports*, 3 (2013) 1988.

819 [46] D.J. Preston, Z. Lu, Y. Song, Y. Zhao, K.L. Wilke, D.S. Antao, M. Louis, E.N. Wang, Heat Transfer
820 Enhancement During Water and Hydrocarbon Condensation on Lubricant Infused Surfaces, *Scientific*
821 *Reports*, 8 (2018) 540.

822 [47] S. Sett, P. Sokalski, K. Boyina, L. Li, K.F. Rabbi, H. Auby, T. Foulkes, A. Mahvi, G. Barac, L.W.
823 Bolton, N. Miljkovic, Stable Dropwise Condensation of Ethanol and Hexane on Rationally Designed
824 Ultrascalable Nanostructured Lubricant-Infused Surfaces, *Nano Letters*, 19 (2019) 5287-5296.

825 [48] X. Dai, B.B. Stogin, S. Yang, T.-S. Wong, Slippery Wenzel State, *ACS Nano*, 9 (2015) 9260-9267.

826 [49] S. Yang, R. Qiu, H. Song, P. Wang, Z. Shi, Y. Wang, Slippery liquid-infused porous surface based
827 on perfluorinated lubricant/iron tetradecanoate: Preparation and corrosion protection application,
828 *Applied Surface Science*, 328 (2015) 491-500.

829 [50] S.B. Subramanyam, G. Azimi, K.K. Varanasi, Designing Lubricant-Impregnated Textured Surfaces
830 to Resist Scale Formation, *Advanced Materials Interfaces*, 1 (2014) 1300068.

831 [51] S. Anand, A.T. Paxson, R. Dhiman, J.D. Smith, K.K. Varanasi, Enhanced Condensation on
832 Lubricant-Impregnated Nanotextured Surfaces, *ACS Nano*, 6 (2012) 10122-10129.

833 [52] D. Daniel, M.N. Mankin, R.A. Belisle, T.-S. Wong, J. Aizenberg, Lubricant-infused micro/nano-
834 structured surfaces with tunable dynamic omniphobicity at high temperatures, *Applied Physics*
835 *Letters*, 102 (2013) 231603.

836 [53] K.-C. Park, P. Kim, A. Grinthal, N. He, D. Fox, J.C. Weaver, J. Aizenberg, Condensation on slippery
837 asymmetric bumps, *Nature*, 531 (2016) 78.

838 [54] X. Zhu, Z. Zhang, X. Men, J. Yang, X. Xu, Rapid Formation of Superhydrophobic Surfaces with Fast
839 Response Wettability Transition, *ACS Applied Materials & Interfaces*, 2 (2010) 3636-3641.

840 [55] P. Zhang, Y. Maeda, F. Lv, Y. Takata, D. Orejon, Enhanced Coalescence-Induced Droplet-Jumping
841 on Nanostructured Superhydrophobic Surfaces in the Absence of Microstructures, *ACS Applied*
842 *Materials & Interfaces*, 9 (2017) 35391-35403.

843 [56] D. Orejon, Y. Maeda, F. Lv, P. Zhang, Y. Takata, Effect of Microstructures on Superhydrophobic
844 and Slippery Lubricant-Infused Porous Surfaces During Condensation Phase-Change, in: *ASME 2018*
845 *16th International Conference on Nanochannels, Microchannels, and Minichannels*, 2018.

846 [57] P. Zhang, F.Y. Lv, A. Askounis, D. Orejon, B. Shen, Role of impregnated lubricant in enhancing
847 thermosyphon performance, *International Journal of Heat and Mass Transfer*, 109 (2017) 1229-
848 1238.

849 [58] S. Zarei, H.R. Talesh Bahrami, H. Saffari, Effects of geometry and dimension of micro/nano-
850 structures on the heat transfer in dropwise condensation: A theoretical study, *Applied Thermal*
851 *Engineering*, 137 (2018) 440-450.

852 [59] L. Liu, F. Xu, L. Ma, Facile Fabrication of a Superhydrophobic Cu Surface via a Selective Etching of
853 High-Energy Facets, *The Journal of Physical Chemistry C*, 116 (2012) 18722-18727.

854 [60] F.Y. Lv, P. Zhang, Fabrication and characterization of superhydrophobic surfaces on aluminum
855 alloy substrates, *Applied Surface Science*, 321 (2014) 166-172.

856 [61] K. Matsumoto, H. Inaba, K. Murahashi, K. Hayashi, D. Shirai, M. Honda, T. Ikeya, K. Matsunaga,
857 Investigation on controlling ice adhesion force to solid surface by using thin film made from silane-
858 coupler, *International Journal of Refrigeration*, 36 (2013) 862-869.

859 [62] D. Quéré, Wetting and Roughness, *Annual Review of Materials Research*, 38 (2008) 71-99.

860 [63] ImageJ, ImageJ 1.50b Wayne Rasband, National Institutes of Health, USA, last checked: April
861 2016, URL <http://imagej.nih.gov/ij>, in.

862 [64] A.F. Stalder, G. Kulik, D. Sage, L. Barbieri, P. Hoffmann, A snake-based approach to accurate
863 determination of both contact points and contact angles, *Colloids and Surfaces A: Physicochemical*
864 *and Engineering Aspects*, 286 (2006) 92-103.

865 [65] S. Sett, X. Yan, G. Barac, L.W. Bolton, N. Miljkovic, Lubricant-Infused Surfaces for Low-Surface-
866 Tension Fluids: Promise versus Reality, *ACS Applied Materials & Interfaces*, 9 (2017) 36400-36408.

867 [66] J.W. Rose, L.R. Glicksman, Dropwise condensation—The distribution of drop sizes, *International*
868 *Journal of Heat and Mass Transfer*, 16 (1973) 411-425.

869 [67] Image-Pro Plus 6.0, Media Cybernetics, Inc., USA, <http://www.mediacy.com/imageproplus>, in.

870 [68] R. Wen, Q. Li, J. Wu, G. Wu, W. Wang, Y. Chen, X. Ma, D. Zhao, R. Yang, Hydrophobic copper
871 nanowires for enhancing condensation heat transfer, *Nano Energy*, 33 (2017) 177-183.

872 [69] J.R. Maa, Drop size distribution and heat flux of dropwise condensation, *The Chemical*
873 *Engineering Journal*, 16 (1978) 171-176.

874 [70] X. Liu, P. Cheng, Dropwise condensation theory revisited: Part I. Droplet nucleation radius,
875 *International Journal of Heat and Mass Transfer*, 83 (2015) 833-841.

876 [71] R. Wen, Z. Lan, B. Peng, W. Xu, X. Ma, Droplet dynamics and heat transfer for dropwise
877 condensation at lower and ultra-lower pressure, *Applied Thermal Engineering*, 88 (2015) 265-273.

878 [72] J.W. Rose, Further aspects of dropwise condensation theory, *International Journal of Heat and*
879 *Mass Transfer*, 19 (1976) 1363-1370.

880 [73] H. Tanaka, Measurements of Drop-Size Distributions During Transient Dropwise Condensation,
881 *Journal of Heat Transfer*, 97 (1975) 341-346.

882 [74] I. Tanasawa, Advances in Condensation Heat Transfer, in: J.P. Hartnett, T.F. Irvine, Y.I. Cho (eds.)
883 *Advances in Heat Transfer*, Vol. 21, Elsevier, 1991, pp. 55-139.

884 [75] N. Watanabe, M. Aritomi, A. Machida, Time-series characteristics and geometric structures of
885 drop-size distribution density in dropwise condensation, *International Journal of Heat and Mass*
886 *Transfer*, 76 (2014) 467-483.

887 [76] C. Yamali, H. Merte Jr, A theory of dropwise condensation at large subcooling including the
888 effect of the sweeping, *Heat and Mass Transfer*, 38 (2002) 191-202.

889 [77] J.W. Rose, Dropwise condensation theory, *International Journal of Heat and Mass Transfer*, 24
890 (1981) 191-194.

891 [78] J. Sun, P.B. Weisensee, Microdroplet self-propulsion during dropwise condensation on lubricant-
892 infused surfaces, *Soft Matter*, 15 (2019) 4808-4817.

893 [79] X. Liu, P. Cheng, Dropwise condensation theory revisited Part II. Droplet nucleation density and
894 condensation heat flux, *International Journal of Heat and Mass Transfer*, 83 (2015) 842-849.

895 [80] V.P. Carey, *Liquid Vapor Phase Change Phenomena: An Introduction to the Thermophysics of*
896 *Vaporization and Condensation Processes in Heat Transfer Equipment*, Second Edition, Taylor &
897 Francis, 2007.

898 [81] N. Miljkovic, R. Enright, E.N. Wang, Modeling and Optimization of Superhydrophobic
899 Condensation, *Journal of Heat Transfer*, 135 (2013).

900 [82] E. Alizadeh-Birjandi, A. Alshehri, H.P. Kavehpour, Condensation on Surfaces With Bipilic
901 Topography: Experiment and Modeling, *Frontiers in Mechanical Engineering*, 5 (2019).

902 [83] N. Miljkovic, E.N. Wang, Condensation heat transfer on superhydrophobic surfaces, *MRS*
903 *Bulletin*, 38 (2013) 397-406.

904 [84] L. Zheng, Y.-X. Wang, J.L. Plawsky, P.C. Wayner, Effect of Curvature, Contact Angle, and
905 Interfacial Subcooling on Contact Line Spreading in a Microdrop in Dropwise Condensation,
906 *Langmuir*, 18 (2002) 5170-5177.

907